The effect of Mn on mineral stability in metapelites revisited: new a–x relations for manganese-bearing minerals

R. W. White[1]*, R. Powell[2] & T. E. Johnson[1]#

[1]Institute of Geoscience, University of Mainz, D-55099 Mainz, Germany

[2]School of Earth Sciences, University of Melbourne, Vic 3010, Australia

[3]Department of Earth Sciences, University of Cambridge, Cambridge, CB2 3EQ, UK

Present address: Department of Applied Geology, The Institute for Geoscience Research (TIGeR), Curtin University, GPO Box U1987, Perth, WA 6845, Australia

*Corresponding author: rwhite@uni-mainz.de

Short title: manganese in metapelites

keywords: garnet; THERMOCALC; Mn-end-members

ABSTRACT

The a–x relations recently presented in White $et\ al.$ 2014, $Journal\ of\ Metamorphic$ $Geology,$ **32**, 261–286 are extended to include MnO. This provides a set of internally consistent a–x relations for metapelitic rocks in the MnO–Na_2O–CaO–K_2O–FeO–MgO– Al_2O_3–SiO_2–H_2O–TiO_2–O_2 (MnNCKFMASHTO) system. The mixing parameters for the Mn-bearing minerals were estimated using the new micro-ϕ approach of Powell $et\ al.$ 2014, $Journal\ of\ Metamorphic\ Geology,$ **32**, 245–260. Then the Mn-end-member thermodynamic properties were calibrated using a database of co-existing minerals involving literature data from rocks and from experiments on natural materials. Mn-end-members were calibrated for orthopyroxene, cordierite, staurolite, chloritoid, chlorite, biotite, ilmenite and hematite, assuming known properties for the garnet end-member spessartine. The addition of MnO to phase diagram calculations results in a marked expansion of the stability of garnet-bearing assemblages. At greenschist facies conditions garnet stability is extended down temperature. At amphibolite facies conditions the garnet-in boundary shifts to lower pressure. While the addition of MnO greatly influences the stability of garnet, it has relatively little effect on the stability of other common metapelitic minerals, with the resultant diagrams being topologically very similar to those calculated without MnO. Furthermore, the addition of MnO in the amounts measured in most metapelites has only a small effect on the mode of garnet, with calculated garnet modes remaining smaller than 1% in the P–T range outside its predicted Mn-free P–T range.

INTRODUCTION

While the key equilibria that control the metamorphic mineral assemblages in metapelites can be shown graphically in systems as simple as K_2O–FeO–MgO–Al_2O_3–SiO_2–H_2O (KFMASH), the quantitative analysis of such rocks using phase equilibria requires larger systems (e.g. White *et al.*, 2000, 2007, 2014; Diener *et al.*, 2007; Smye *et al.*, 2010). These larger systems are necessary to accomodate relatively minor components such as TiO_2, Na_2O, CaO Fe_2O_3 and MnO that nevertheless may exhibit a strong influence over the stability of certain common minerals. For example, TiO_2 is known to strongly affect the stability of biotite at higher temperature.

Manganese is well known to affect mineral assemblages in metasedimentary rocks via its strong stabilising effect on garnet (e.g. Atherton, 1964; Osberg, 1971; Symmes & Ferry, 1992; Droop & Harte, 1995; Mahar *et al.*, 1997; Tinkham *et al.*, 2001). Thus, despite its typically low concentration (≈ 0.1–0.3 wt %) in metasediments (e.g. Ague, 1991; Atherton & Brotherton, 1982) manganese forms a critical component in phase equilibria and the interpretation of metamorphic assemblages (e.g. Symmes & Ferry, 1992; Droop & Harte, 1995; Mahar *et al.*, 1997). Calculations in manganese-free systems ranging from KFMASH to NCKFMASHTO (Na_2O–CaO–K_2O–FeO–MgO–Al_2O_3–SiO_2–H_2O–TiO_2–O_2) show a relatively restricted stability of garnet, even in relatively Fe-rich bulk compositions (e.g. Powell *et al.*, 1998; White *et al.*, 2000, 2014). For example, the NCKFMASHTO calculations presented in White *et al.* (2014) for the amphibolite facies average metapelite composition from Ague (1991) have garnet stability restricted to pressures above ≈ 7.5 kbar and temperatures above ≈ 570 °C. These calculations contrast markedly with the common occurence of manganese-bearing garnet in many greenschist and amphibolite facies rocks, including those from contact aureoles and low-P Buchan type terrains (e.g. Harte & Hudson, 1979; Hudson, 1985; Pattison & Tinkham, 2009)

Some of the first studies to undertake quantitative phase diagram calculations beyond the KFMASH system (e.g. Spear & Cheney, 1989; Symmes & Ferry, 1992; Mahar *et al.*, 1997) incorporated Mn-end-members in the calculations in order to better predict the stability of garnet. While a large number of studies since have considered MnO in phase diagram calculations in various systems (e.g. Tinkham & Ghent, 2005; White *et al.*, 2005; Wei *et al.*, 2007; Pattison & Tinkham, 2009), these studies generally did not involve the

development of new thermodynamic models or recalibration of the Mn end-member data. For example the a–x relations presented in Tinkham et $al.$ (2001) and Tinkham & Ghent (2005), are simply the combination of the Mahar et $al.$ (1997) MnO relationships to the extant Mn-free a–x relations of the time (e.g. Holland et $al.$, 1998; Holland & Powell, 1998; Powell & Holland 1999; White et $al.$, 2000). Obviously this is not a defensible approach given that the underlying formulation of the Mahar et $al.$ (1997) a–x relationships was ideal mixing, while the later models with which they were combined involved the symmetric formalism. Thus, there were large inherent inconsistencies in the a–x relations used in these previous studies.

In this paper we develop new end-member properties for the MnO-bearing end-members following a similar approach to Mahar et $al.$ (1997). This builds on and extends the thermodynamic descriptions of White et $al.$ (2014) and they are compatible with the most recent Holland & Powell (2011) dataset. Thus, for the first time since 1997, the thermodynamic properties of the manganese end-members for phases are consistent with the other end-members in each phase.

THE THERMODYNAMICS OF MN-BEARING MINERALS

The following phases, with their phase abbreviations, are considered to be Mn-bearing: garnet (g), orthopyroxene (opx), cordierite (cd), staurolite (st), chlorite (chl), chloritoid (ctd), biotite (bi), and ilmenite (ilm). The manganese end-members of these minerals are the same as those whose properties appear in `ds6` (Holland & Powell, 2011), except for the manganese end-member of orthopyroxene which is made from the dataset end-member, pyroxmangite ($MnSiO_3$): garnet (spessartine, spss, $Mn_3Al_2Si_3O_{12}$), biotite (mnbi, $KMn_3AlSi_3O_{10}(OH)_2$), orthopyroxene (mnopx, $Mn_2Si_2O_6$), cordierite (mncrd, $Mn_2Al_4Si_5O_{18}$), staurolite (mnst, $Mn_4Al_{18}Si_{7.5}O_{44}(OH)_4$), chloritoid (mnctd, $MnAl_2SiO_5(OH)_2$), chlorite (mnchl, $Mn_5Al_2Si_3O_{10}(OH)_8$) and ilmenite (pyrophanite, pnt, $MnTiO_3$).

In biotite, orthopyroxene and chlorite, manganese is distributed across non-equivalent octahedral sites such that the site fraction of Mn is the same on the different sites (coined equidistribution). Note that this is not equipartition, which in this case might mean making Mn/Fe^{2+} the same across the sites. Unlike equipartition, equidistribution is not

thermodynamically inconsistent (Holland & Powell, 2007). While it is likely that Mn is partitioned between the non-equivalent sites as Mg and Fe^{2+} are, rather than equally distributed, such an approach would require additional ordered manganese end-members, and the enthalpy of ordering would need to be estimated. Although approaches to implement this are available, e.g. Powell *et al.* (2014), given the lack of data on Mn ordering and the fact that Mn is nearly always a minor constituent of these phases, the additional complexity of such an approach is not considered to be warranted.

The formulation of the a–x relations of the minerals involves ideal-mixing-on-sites and the symmetric formalism (Powell & Holland, 1993; Powell *et al.*, 2014). The parameterisation follows White *et al.* (2014) closely, with the addition of the non-ideality involving Mn substitution in the minerals remaining to be considered. Except for garnet and ilmenite, there are no experimental data that would allow the pairwise macroscopic interaction energies (W) between the manganese and the other end-members in the minerals to be estimated. As argued in Powell *et al.* (2014), the simplification of assuming that all the interaction energies, W, involving the manganese and other end-members are zero is unlikely to be correct, and is likely to bias the results of calculations. Given that even Mg–Fe^{2+} interactions have significant non-zero W, it is much better to give the a–x relations involving Mn a good "shape", with non-zero W. A way to do this is presented in Powell *et al.* (2014), referred to as micro-ϕ (see below), and this approach has already been used to generate most of the W involving ferrous end-members in the minerals in White *et al.* (2014). Once the shape is established, what remains to be determined is the enthalpy adjustment (ΔH, or DQF in THERMOCALC parlance) of the manganese end-members already in the dataset (Holland & Powell, 2011), which involves the "historical" values relating to the ideal-mixing-on-sites approach of Mahar *et al.* (1997).

In micro-ϕ, the idea is to implement an expectation that the a–x relations for the X–Y subsystem of a mineral be related to the those of the Mg–Al subsystem, commonly the subsystem that is best known experimentally. In this X might be, for example, Fe^{2+} or Mn, and Y, Fe^{3+} or Cr. Here, the microscopic w of the X–Y subsystem is made proportional to the Mg–Al subsystem with the proportionality represented by ϕ. This allows the X–Y subsystem to be easily made less ($\phi < 1$) or more ($\phi > 1$) non-ideal than the Mg–Al subsystem. The implementation of micro-ϕ starts with disassembling the macroscopic W into their constituent microscopic same-site and cross-site w that arise

from pairwise interactions between the cations on the sites in the mineral (Powell & Holland, 1993). Then simplifications and approximations are made to these w using heuristics[1], before reassembling the macroscopic W. In Powell *et al.* (2014) and White *et al.* (2014), with $X = Fe^{2+}$ and $Y = Fe^{3+}$, the main heuristic values allowing parameterisation of the a-x relations are;

$$
\begin{aligned}
\phi &= 0.7 \\
\phi_3 &= 0.8 \\
w_{FeMg,oct} &= 4 \text{ kJ} \\
w_{MgAl,oct} &= 10 \text{ kJ},
\end{aligned}
\tag{1}
$$

in which ϕ has the effect, $w_{FeX,oct} = \phi\, w_{MgX,oct}$, where Mg, Fe^{2+}, and X are mixing on the octahedral site, oct. Thus, the Fe subsystem of a mineral can be made to have non-ideality that is proportional to that of the Mg subsystem with the proportionality arising from ϕ. Similarly, ϕ_3 has the effect, $w_{YFe3,oct} = \phi_3\, w_{YAl,oct}$, the Fe^{3+} subsystem being made to have non-ideality that is proportional to that of the Al subsystem. In this way, for example, $w_{FeFe3,oct} = \phi\, \phi_3\, w_{MgAl,oct}$. The two final values above are the microscopic interaction energies. These are discussed in detail in Powell *et al.* (2014), along with the additional necessary approximations involving the cross-site microscopic interaction energies.

If X is Mn, then ϕ_{Mn} needs to be specified, the following chosen heuristics being discussed below

$$
\begin{aligned}
\phi_{Mn} &= 0.7 \\
w_{FeMn,oct} &= 2 \text{ kJ}
\end{aligned}
\tag{2}
$$

making $w_{MgMn,oct} \approx 2.9$ kJ, or rounded to 3 kJ for phases where little is known about the overall a–x relations of the mineral, keeping the W as whole numbers. Here, as opposed to the above, the value for $w_{FeMn,oct}$ is taken as known and the micro-ϕ approach is used to derive the value for $w_{MgMn,oct}$. Regarding the behaviour of Mn in mixing with Fe^{2+} and Mg, the data is very limited and no data exists for directly constraining Mn mixing properties involving octahedral sites in silicates. However, there is some information regarding garnet and ilmenite, through experiments on Fe–Mn exchange experiments (Pownceby *et al.*, 1987; Feenstra & Peters, 1996). As recognised by Pownceby *et al.* (1987), the sundry correlations

---

[1]Heuristic is used here in the sense of an experience-based rule of thumb or educated guess, commonly in the context of providing a numerical value for a parameter or a relationship between parameters

between controlling thermodynamic parameters means that separating information about garnet from that of ilmenite via the experimental data is difficult. However, Pownceby *et al.* (1987) do argue that Fe–Mn interactions have to be slightly stronger in ilmenite than in garnet: they suggest on a single site basis $W_{\text{FeMn}}^{\text{ilm}} - \frac{1}{3}W_{\text{FeMn}}^{\text{g}} \approx 1.2$ kJ. Separately, O'Neill (1998) estimated from Fe–Mn exchange between ilmenite and olivine that $W_{\text{FeMn}}^{\text{ilm}} = 1.8 \pm 0.1$ kJ, with provisos about the thermodynamics of olivine. This value is also consistent with O'Neill *et al.* (1989), who derived $W_{\text{FeMn}}^{\text{ilm}} = 2.2 \pm 0.3$ kJ. This leads to our adoption of $W_{\text{FeMn}}^{\text{ilm}} = 2$ kJ. This then leads to $W_{\text{alm,spss}} = 3(W_{\text{FeMn}}^{\text{ilm}} - 1.2) \approx 2$ kJ.

Recently, Dachs *et al.* (2014) undertook a detailed analysis of Fe–Mn mixing in garnet and suggested almandine-spessartine mixing is asymmetric and a little more non-ideal than that adopted here, for more almandine-rich garnet. In the light of the discussion of the various experimental data by O'Neill (1998), adoption of the simpler, symmetric, model is defensible. Making the unavoidable step of carrying this value across to octahedral sites in silicates, leads to $w_{\text{MgMn,oct}} = 3$ kJ, once ϕ_{Mn} is chosen to be 0.7, given that this w is likely to be of the same order as $w_{\text{MgFe,oct}}$. The interaction energies that result from the adoption of these heuristics are given in Appendix 1. They should be seen in the context of the Appendix in White *et al.* (2014) for the way in which the approach of Powell & Holland (1993) and Holland & Powell (1996ab) for writing a-x relations is implemented.

The dataset of Holland & Powell (2011) contains data for all the manganese end-members above but their enthalpies are based on the original ideal-mixing calculations of Mahar *et al.* (1997). As these are superceded by the non-ideal mixing calculations presented here, the enthalpies of these end-members need to be modified. A reference point is provided by the properties of the pyrophanite and spessartine dataset end-members (Holland & Powell, 2011), as they are based on experimental data rather than being from Mahar *et al.* (1997). They provide an anchor for establishing manganese end-member properties for the other minerals. As in Mahar *et al.* (1997), the approach taken is to use Mg–Mn exchange reactions between the minerals using a natural assemblage database constructed for the purpose (Appendix 2). The database used for calibration is presented as Supplementary Information. Exchange reactions are good for calibration purposes as the resulting thermodynamic properties are not sensitive to the chosen P–T of the natural assemblages. This is the converse of saying that exchange reactions make bad thermometers because they are so sensitive to the thermodynamics. Such thermometers can easily lead to

180 strong bias in thermometric results (e.g. through poor thermodynamic formulation or

181 when ferric is ignored), e.g. Powell & Holland (2008). The exchange reactions used are the

182 Mg–Mn ones so as to minimise the consequences of difficulties with respect to ferric iron.

183 The derivation of the enthalpy modifications of the dataset via the Mn–Mg exchange

184 reactions is given in Appendix 3, completing the thermodynamic descriptions of the phases.

PHASE DIAGRAM CALCULATIONS

186 The phase diagrams presented here using the new a–x relations were calculated using

187 THERMOCALC version 3.37 and the internally-consistent end-member dataset of Holland &

188 Powell (2011), ds62 (created 6th February 2011). Calculations were undertaken in a range

189 of chemical systems ranging from MnO–K_2O–FeO–MgO–Al_2O_3–SiO_2–H_2O (MnKFMASH)

190 to MnO–Na_2O–CaO–K_2O–FeO–MgO–Al_2O_3–SiO_2–H_2O–TiO_2–O_2 (MnNCKFMASHTO).

191 The version of the Holland & Powell dataset used here is slightly newer than that used in

192 White *et al.* (2014) for modelling in NCKFMASHTO (ds61), though the differences in the

193 resulting diagrams from this are very minor.

194   In addition to the Mn-bearing minerals, garnet, orthopyroxene, cordierite, staurolite,

195 chlorite, chloritoid, biotite and ilmenite, the following minerals were considered in the

196 phase diagram calculations: sillimanite/kyanite/andalusite (sill/ky/and), spinel (sp),

197 muscovite (mu), paragonite (pa), margarite (ma), K-feldspar (ksp), plagioclase (pl), albite

198 (ab), epidote (ep), sphene (sph), magnetite (mt), rutile (ru), quartz (q) and melt (liq). For

199 the minerals not considered to be Mn-bearing, the a–x relationships of White *et al.* (2014)

200 were used for the white micas and silicate melt; Holland & Powell (2003) for feldspar,

201 White *et al.* (2000) for magnetite at subsolidus conditions, White *et al.* (2002) for

202 magnetite and spinel at suprasolidus conditions, and Holland & Powell (2011) for epidote.

MnKFMASH

P–T Projections and compatibility diagrams

205 In adding MnO to the KFMASH system, each of the invariant points in KFMASH becomes

206 a univariant line extending away from the KFMASH invariant, typically to lower P–T

207 conditions. The Mn content of the phases increase away from the invariant point. Where

8

the KFMASH invariant point is garnet bearing, the univariant that emanates from it may extend a considerable distance in P–T. By contrast, MnKFMASH univariant reactions that lack garnet typically only extend a short distance from their KFMASH origins before garnet appears at a new MnKFMASH invariant. A MnKFMASH grid is shown in Fig. 1 for subsolidus (450 °C) to suprasolidus (950 °C) conditions. The Mn content of garnet $(m(g))$ along four of the univariant reactions is shown via the horizontal ticks along each reaction. The grid is relatively simple with only two invariant points. The suprasolidus univariant reactions extend only a short distance from their KFMASH origins before terminating in another subsystem. The first invariant point [opx cd ksp liq]—using the [absent phase] notation—occurs at ≈0.8 kbar and ≈480 °C and links the main univariant reactions seen in the subsolidus part of the grid. Details of the reactions that emanate from this point are shown in the oval shaped inset in Fig. 1. The second invariant point [opx st chl ctd] occurs where the muscovite breakdown reaction intersects the wet solidus (≈5.8 kbar, ≈725 °C). For P–T conditions below the solidus and the muscovite breakdown reaction there are four univariant reactions that could be seen under typical crustal metamorphic conditions. These reactions, in order of increasing T are;

$$als + ctd = g + st + chl, \tag{3}$$

$$chl + ctd = g + st + bi, \tag{4}$$

$$st + chl = g + als + bi \tag{5}$$

and

$$g + als + chl = cd + bi, \tag{6}$$

where als represents the stable aluminosilicate of and, sill and ky. A singularity occurs along reaction 6 involving als swapping sides of the reaction at lower pressure. For reactions 3–5, which all emanate from KFMASH invariant points, each represents a garnet-bearing equivalent to the garnet-absent reaction from each KFMASH invariant (White *et al.*, 2014), with the KFMASH and MNKFMASH reactions typically occuring only a few degrees apart for most of their length because the incorporation of Mn is minor

9

in all of the phases apart from garnet. As a consequence, the garnet-absent assemblage possible for each MnKFMASH reaction (e.g. ky–st–ctd–chl for below reaction 3) typically has a very limited P–T stability range between the KFMASH and MNKFMASH reactions.

The phase relationships relating to the low variance MnKFMASH equilibria (with $v = 1$–3) can also be shown in compatibility diagrams, that additionally show the composition space that these equilibria occupy. A series of AFM and MnFM compatibility triangles are shown in Fig. 2 and Fig. 3 respectively for the P–T conditions shown on Fig. 1 as small triangles. The AFM triangles (Fig. 2) have garnet, quartz, muscovite and H_2O in excess and the MnFM diagrams (Fig. 3) have aluminosilicate, quartz, muscovite and H_2O in excess.

The AFM compatibility diagrams are shown for an isobaric transect at 4.5 kbar (Fig. 2a–f) at the P–T conditions shown as open triangles in Fig. 1. As garnet is taken as in-excess, these diagrams show the changing stable divariant to quadrivariant equilibria amongst the remaining ferromagnesian phases and aluminosilicate. The sequence of AFM diagrams shows the changes in stable tie-triangles on crossing each of the univariant reactions 3–5. For example Fig. 2a and Fig. 2b illustrate the breakdown of the ky–ctd tie-line and the formation of the st–chl tie line on crossing reaction 3, with the phases involved having very similar compositions to those expected in the MnO-free system.

The mineral composition relationships either side of reaction 3 are shown in a sequence of MnFM compatibility triangles (Fig. 3) calculated for pressures of 12 kbar and 6 kbar (filled triangles on Fig 1). These diagrams show the varying size of the garnet one-phase field as a function of pressure along the reaction. As these diagrams are calculated with kyanite in excess, they are only appropriate for rather aluminous compositions. For the diagrams at 12 kbar (Fig. 3a, b), the garnet one-phase field is relatively large and extends a considerable distance from the MnO apex towards the FeO apex. Chlorite, staurolite and, where present, chloritoid all plot at low MnO contents. Thus, rocks with only small amounts of MnO may contain garnet at these conditions. At T below the reaction, two stable divariant assemblages occur (g–st–ctd and g–chl–ctd). As discussed above, the garnet-absent tie triangle (st–ctd–chl) is not stable at these conditions, but appears from the base of the compatibility triangle less than 0.1 °C below the MnKFMASH univariant. Above the reaction only one stable tie triangle exists, and, as kyanite is in excess, this reaction is a terminal chloritoid reaction.

²⁶² The diagrams at 6 kbar (Fig. 3c, d) show substantially reduced garnet one-phase fields

²⁶³ in comparison with those at 12 kbar and the other phases (especially staurolite and

²⁶⁴ chloritoid) may incorporate substantially more MnO before garnet must become stable.

²⁶⁵ Thus, garnet is limited to somewhat higher bulk rock MnO contents and is considerably

²⁶⁶ more MnO rich than at higher P.

Pseudosections

²⁶⁸ The MnKFMASH system is useful for demonstrating the effect of adding MnO on the

²⁶⁹ stability of key assemblages. Figure 4 shows the predicted assemblages for three different

²⁷⁰ bulk compositions with different $x_{Fe} = FeO/(FeO + MgO)$ and $x_{Al} = Al_2O_3/(Al_2O_3 + FeO$

²⁷¹ $+ MgO)$ proportions. Figure 4a is a P–T pseudosection from 450 °C to 950 °C and for the

²⁷² same composition as used for fig. 4 in White *et al.* (2014) but with 0.1 mol. % MnO.

²⁷³ Pseudosections are also presented for subsolidus conditions for a more magnesian

²⁷⁴ composition (Fig. 4b) and a more magnesian and more aluminous composition (Fig. 4c),

²⁷⁵ each with an MnO content of $\approx$ 0.1 mol. % (see Table 1 for exact compositions used). The

²⁷⁶ two lower x_{Al} pseudosections (Fig. 4a, b) are topologically similar, containing largely the

²⁷⁷ same assemblage fields.

²⁷⁸ The pseudosections are dominated by divariant to quadrivariant fields. However, a

²⁷⁹ short segment of the MnKFMASH reaction 5 is seen in each pseudosection. This reaction

²⁸⁰ controls the disposition of the main divariant fields seen in each diagram. Each of these

²⁸¹ divariant fields is equivalent to a univariant equilibria stable in the KFMASH system and

²⁸² are little displaced in P–T from the KFMASH univariants. For example the divariant

²⁸³ g–st–chl–bi field in each pseudosection is equivalent to the KFMASH univariant reaction:

$$g + chl = st + bi. \tag{7}$$
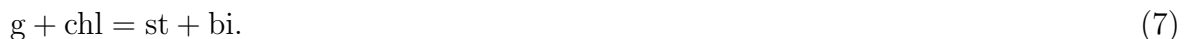
²⁸⁴ In Fig. 4, the garnet-in lines for a bulk rock MnO content of 0.05 (dashed red line

²⁸⁵ labelled MnO=0.05) and for the MnO-free system (red line labelled MnO=0) are also

²⁸⁶ shown. These garnet-in lines illustrate the relationship between the bulk MnO content and

²⁸⁷ the P–T stability of garnet, with the garnet-in lines moving down T and P relative to the

²⁸⁸ MnO-absent garnet-in lines. At lower T (greenschist facies) the garnet-in boundaries are

²⁸⁹ relatively steep such that the main effect of adding MnO is a shift to lower T of the

²⁹⁰ garnet-in line. Under amphibolite facies conditions, the garnet-in line is somewhat flatter

11

²⁹¹ such that the main effect of adding MnO is to increase garnet stability down P. The

²⁹² combination of these two features results in the greatest displacement of the garnet-in line

²⁹³ occurring at close to 500 °C where it forms a distinct wedge that may extend to the base of

²⁹⁴ the diagram. Thus, at low P the calculations predict the appearance of garnet soon

²⁹⁵ followed by its disappearance. However, in reality, such a narrow field could conceivably be

²⁹⁶ crossed with no garnet growth having occurred.

²⁹⁷ A noticeable feature of all three pseudosections is the small triangular field of

²⁹⁸ garnet-absent assemblages within the overall garnet stability field. These garnet-absent

²⁹⁹ fields each emanate from the divariant g–st–chl–bi fields in Figs 4a–c and reflect the fact

³⁰⁰ that garnet is a reactant in reaction 7. The high-T boundary of this garnet absent field is

³⁰¹ defined by the equivalent to the garnet producing KFMASH reaction,

$$\text{st} = \text{g} + \text{als} + \text{bi}. \tag{8}$$

³⁰² Thus, along a prograde path, the calculations predict the appearance, disappearance and

³⁰³ reappearance of garnet.

³⁰⁴ While the stability of subsolidus garnet-bearing assemblages is strongly influenced by

³⁰⁵ MnO, the high temperature assemblages are significantly less so. At temperatures above

³⁰⁶ about 750 °C the addition of 0.1 mol. % MnO to the bulk rock composition stabilises

³⁰⁷ garnet down pressure by less than 1 kbar (Fig. 4a). For upper amphibolite facies

³⁰⁸ conditions, manganese can have significant effect on garnet stability, particularly at 3–5

³⁰⁹ kbar where the presence of MnO may substantially extend g–sill–bi and

³¹⁰ g–sill–cd–bi-bearing assemblages to lower P–T.

MnNCKFMASHTO

³¹² The addition of MnO to the NCKFMASHTO calculations presented in White *et al.* (2014)

³¹³ results in the MnNCKFMASHTO system that closely approximates the composition space

³¹⁴ of natural metapelites. Thus, this system is potentially useful for applied phase equilibria

³¹⁵ modelling studies.

³¹⁶ Figure 5 is a P–T pseudosection based on the composition used for fig. 5b presented in

³¹⁷ White *et al.* (2014), but with 0.1 mol % MnO. Garnet-in lines are additionally shown for

³¹⁸ the MnO-free system and for MnO contents of 0.05 and 0.15. As with the MnKFMASH

³¹⁹ calculations, the addition of MnO has a profound affect on the stability of garnet with

12

320 garnet-bearing assemblages stabilised to lower P and T. Otherwise, Fig. 5 is very similar

321 to the equivalent pseudosection in White et al. (2014), with the same main assemblages

322 present. Garnet-bearing assemblages are limited to pressures above about 7 kbar and

323 temperatures above about 550 °C for the MnO-free system but stabilised to pressures as

324 low as 2 kbar and temperatures close to 500 °C with 0.1 mol % MnO. As with the

325 MnKFMASH calculations, the main effect of adding MnO is to lower the temperature of

326 garnet stability in greenschist-facies assemblages and to lower the pressure of garnet

327 stability in amphibolite-facies assemblages. At pressures above 2 kbar, garnet first appears

328 in a series of g–chl–bi-bearing fields that may additionally involve combinations of

329 paragonite, epidote, plagioclase, ilmenite and magnetite. At higher temperature, the lower

330 pressure limit of garnet-bearing assemblages involves g–and–bi- and g–sill-bi-bearing

331 assemblages, in contrast to its restriction to ky-bearing assemblages in the MnO-free

332 system. A small, triangular garnet-absent field is also present in Fig. 5 related to the

333 higher variance equivalent to reaction 7.

334   Figure 6 shows the phase relations for a more aluminous composition, based on that of

335 fig. 7 in White *et al.* (2014). As with the pseudosection in fig. 7 of White *et al.* (2014),

336 Fig. 6 contains a series of chloritoid-bearing fields, a restricted stability range for biotite

337 and an enhanced stability field for the aluminosilicates compared with Fig. 5. At pressures

338 above about 4 kbar, the first appearance of garnet occurs in a series of biotite-absent

339 assemblages involving combinations of garnet, chlorite, staurolite and chloritoid. Under

340 greenschist-facies conditions the effect of MnO on garnet stability is less profound than in

341 the less aluminous composition, with the garnet-in line moving down T by about 30 °C

342 with the addition of 0.1 mol. % MnO. A large embayment in the garnet-in boundary exists

343 at close to 4 kbar, with the garnet-in line trending from about 540 °C at $\approx$ 3.8 kbar up to

344 about 640 °C at $\approx$ 5.8 kbar before trending back down P and T to about 510 °C and 1.6

345 kbar. This embayment can also be seen in the garnet-in line for the bulk MnO content of

346 0.05 mol. %, shown as a dashed red line. Like with the triangular garnet-absent fields

347 described above, this embayment is controlled by the higher variance equivalents of

348 reaction 7 consuming garnet and reaction 8 producing it.

349   Ague (1991) compiled two average metapelite compositions, one for greenschist facies

350 metapelites and one for amphibolite facies metapelites. Although these two compositions

351 are broadly similar, there are notable differences in composition between the two, including

in the bulk MnO content (Ague, 1991). In comparison with the compositions used above, the average metapelite compositions in Ague (1991) have higher CaO and Na_2O contents, but are otherwise similar to the composition used for Fig. 5, albeit with a lower x_{Fe}.

Figure 7 is a P–T pseudosection for the low-grade composition from Ague (1991). A small adjustment to the CaO content was made to account for the likely presence of apatite and the $Fe_2O_3/(FeO + Fe_2O_3)$ ratio was arbitrarily set at 0.077. For Fig. 7, the MnO content (0.284 mol. %) is higher than that used in the preceding diagrams (0.1) so that most of the diagram is garnet-bearing. Garnet-absent assemblages are restricted to a small window in the bottom left of the diagram and a second at low pressure at $T > 500$ °C. The garnet-in lines for bulk MnO contents of 0.15 and 0.05 mol. % are additionally shown on the diagram. These two garnet-in lines are similar in shape and position to the equivalent ones in Fig. 5. Topologically, the disposition of the main AFM ferromagnesian assemblages in Fig. 7 is similar to that in Fig. 5, with the exception of the extent of garnet stability and, due to the more magnesian composition for Fig. 7, the appearance of kyanite-bearing fields in Fig. 7. As with the NCKFMASHTO calculations presented in White et $al.$ (2014), the large number of potential phases stable in these diagrams allows for the possibility of univariant reactions to be stable. In Fig. 7 short segments of two univariant reactions are seen at conditions close to 6 kbar and 540–580 °C and are linked by narrow divariant fields. Each of these univariant reactions involve nine phases (excluding in-excess phases) and are dominated by large reaction coefficients for the micas and plagioclase and relatively small coefficients for the ferromagnesian phases and the oxide phases, with the exception of biotite. For example the higher temperature reaction of the two at 5.6 kbar is,

$$44g + 1315bi + 3645pa + 1363ma = 227st + 540chl + 3617pl + 92ilm + 10mt. \tag{9}$$
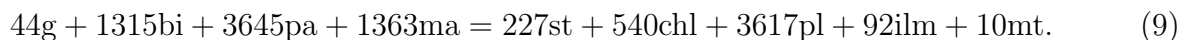
Given the issues outlined in White et $al.$ (2014) regarding margarite stability it is possible that the presence of these two univariants in the pseudosection is anomalous, though they may be stable in a grid.

A P–T pseudosection for the amphibolite-facies metapelite composition from Ague (1991) is shown in Fig. 8. Here, the $Fe_2O_3/(FeO + Fe_2O_3)$ ratio was set at 0.081 but the CaO content was not reduced. The MnO content (MnO = 0.175) is lower than that for Fig. 7, resulting in a more restricted field for garnet stability. The two univariant reactions present in Fig. 7 are also seen in this bulk composition and both diagrams are topologically very similar in terms of the main assemblage fields. As with many of the other

14

pseudosections, a small garnet-absent field occurs within the larger area of garnet presence. Garnet-in lines are additionally shown for bulk MnO contents of 0, 0.05, 0.1 and 0.15 mol. %. As with the diagrams presented earlier, the addition of MnO drives the garnet-in line down T under greenschist facies conditions and down P under amphibolite facies conditions, with a wedge-shaped pressure minima for garnet at approximately 2 kbar and 520 °C involving the assemblage g–and–chl–bi–pl–ilm–mt. In the MnO free system the stability of garnet-bearing assemblages is restricted to pressures above about 7.5 kbar (see White $et\ al.$ (2014, fig. 11) for the corresponding NCKFMASHTO pseudosection).

The effect of MnO at higher metamorphic grades is shown on a P–T pseudosection (Fig. 9) calculated for the amphibolite-facies metapelite composition from Ague (1991). Under amphibolite-facies conditions MnO exerts a significant effect on the stability of garnet-bearing assemblages. At temperatures below the muscovite breakdown reaction, the addition of 0.175 mol. % MnO shifts the garnet in line down approximately 3 kbar relative to the MnO-absent system. Between the muscovite breakdown reaction and the first appearance of cordierite, the garnet-in line is steep and displaced close to 80 °C down T relative to the manganese-free system. Overall this greatly expands the P–T range of g–sill–bi-bearing assemblages relative to that in the MnO-free system. At temperatures above the appearance of cordierite the effect of adding MnO is less profound, with, for example, the garnet in line now located less than 1 kbar lower than for the MnO-free system at 850 °C.

The effect of considering MnO in calculations can be further addressed via T–x_{MnO} and P–x_{MnO} pseudosections such as Fig. 10, based on the greenschist-facies composition from Ague (1991). Figure 10a is a T–x_{MnO} pseudosection constructed for a pressure of 6 kbar to illustrate the down-temperature shift of the garnet-in line as a function of MnO content. The x axis varies from MnO = 0 to MnO = 0.3 mol %. At low MnO contents ($x < 0.15$) garnet is absent from the assemblages over the whole temperature range considered. The garnet-in line generally trends to lower T with increasing MnO, but with several switch-backs, especially at temperatures above 590 °C, a feature that can also be seen in the garnet-in line for MnO = 0.05 in Fig. 7.

A P–x_{MnO} pseudosection calculated for a temperature of 580 °C for the same composition range is shown in Fig. 10b and shows the down-pressure shift of the garnet-in line as a function of bulk rock MnO content. In the MnO-free system, garnet-bearing

15

assemblages are restricted to pressures of above 8.5 kbar for this composition but get as low as 1.5 kbar for MnO contents above 0.27 mol %. A switch-back in the garnet-in line occurs at close to 4 kbar related to the up pressure consumption of garnet through the higher-variance equivalent of reaction 8. In both the T–x_{MnO} and P–x_{MnO} pseudosections the P and T conditions for the main assemblages are little influenced by the consideration of MnO with most assemblages forming near horizontal bands across each diagram.

The pseudosections in Fig. 10 are also contoured for garnet mode. The garnet mode contours in both diagrams broadly parallel the garnet-in boundary reflecting the variable consumption or production of garnet as P or T conditions evolve. For Fig. 10a garnet is not stable for low MnO contents, such that the garnet-bearing assemblages in the diagram are a direct consequence of the addition of MnO. Despite the large increase in the overall stability of garnet-bearing assemblages, the addition of MnO results in only small proportions of garnet being stable ($< 3\%$) for the highest bulk MnO contents considered here. The maximum garnet contents are achieved at temperatures just below 590 °C at the low-T boundary (st-out) of the assemblage g–st–bi–pa–ma–pl–ilm–mt. For temperatures below this, relatively little garnet is produced for close to 50–100 °C above the garnet-in line. For example, at $x = 0.5$ garnet proportions only reach 1% approximately 100 °C above the initial appearance of garnet.

For the P–x_{MnO} pseudosection Fig. 10b the garnet mode contours are similarly sub parallel to the garnet-in line. However, unlike the T–x_{MnO} pseudosection garnet does become stable in the MnO-free system at about 8.5 kbar. As with the T–x_{MnO} diagram, the mode of garnet remains low for a considerable pressure above the garnet in line. For example at $x = 0.7$ the calculations predict less than 1% garnet for 3 kbar above the initial appearance of garnet. However, at higher MnO contents garnet modes above 4% are possible. In general, the mode of garnet increases with increasing pressure with the exception of the narrow field (g–sill–st–bi–pl–ilm–mt) across which garnet is consumed. A notable increase in the mode of garnet occurs across the narrow set of divariant fields and the section of univariant equilibria (at $x < 0.75$) close to 5.6 kbar.

DISCUSSION AND CONCLUSIONS

The extension of the NCKFMASHTO a–x relations presented in White *et al.* (2014) to include MnO provides a chemical system for phase diagram calculations (MnNCKFMASHTO) that closely matches that of natural metapelites and metapsammites. Importantly, the a–x relations in both MnO-bearing and MnO-absent systems are thermodynamically consistent, with the Mn-end-member properties calibrated in concert with the a–x relations presented in White *et al.* (2014). This contrasts with many previous sets of MnO-bearing a–x relations in which the Mn-end-member properties (DQF adjustments) from Mahar *et al.* (1997) were coupled with the extant version of the Holland & Powell end-member dataset and NCKFMASHTO a–x relations of the time. This resulted in inherent inconsistencies within the models, with such inconsistencies becoming more problematic as the NCKFMASHTO a–x relations evolved. The thermodynamic descriptions of the Mn-bearing minerals are built on the a–x development approach referred to as micro-ϕ of Powell *et al.* (2014), as detailed in the body of the paper and in Appendix 1. This approach is designed for situations where little is known about the a–x relations, which is true for Mn incorporation in the the minerals being considered here, apart from garnet and ilmenite. Once the a–x relations were established the enthalpy modifications to the dataset properties of Holland & Powell (2011) were derived from a large database of natural coexisting minerals in metapelites (see Appendix 2–3).

The components of the MnNCKFMASHTO system commonly account for more than 98% of the mass of common metapelitic to metapsammitic rocks. Despite being a relatively minor component of metapelites, MnO exerts an important influence on the P–T stability of garnet-bearing assemblages. Other than the stabilisation of garnet, the presence of MnO has little effect on the P–T conditions of common assemblages. At higher grades, the effect of MnO on the P–T extent of garnet-bearing assemblages is less profound, as most metapelite compositions will be garnet-bearing regardless at such conditions. Thus, for many high-T studies, inclusion of MnO is likely to have little effect on the resulting estimates of P–T conditions, unless the appearance or absence of garnet is of central importance. However, for modelling of transitional amphibolite to granulite facies assemblages or high-grade metamorphism at low pressures, consideration of MnO may strongly influence the interpretation of P–T conditions.

17

Although MnO greatly expands garnet stability to lower P–T conditions, the resulting mode of garnet commonly remains low until higher variance equivalents to garnet-producing KFMASH reactions are crossed. This can be seen in Fig. 10 which is contoured for garnet mode. Thus, garnet-rich rocks metamorphosed at P–T conditions outside the MnO-free stability field of garnet are likely to be rather rich in MnO compared to typical metapelites.

The phase diagrams presented here reproduce the main assemblages seen in common metapelites, at least for typical MnO contents MnO < 0.3 wt % (e.g. Ague 1991; Atherton and Brotherton, 1982). Furthermore, using the amphibolite facies average metapelite composition from Ague (1991) as an example (Fig. 8), key features such as the garnet, staurolite, kyanite and silimanite isograds occur in the correct order along typical metamophic field gradients inferred for barrovian metamorphism, with the biotite isograd occurring off the diagram at $T = 400$–450 °C. For higher MnO contents, such as in Fig. 7, the garnet and biotite isograds could potentially swap positions but the other isograds would be unaffected.

In application, these models may be less reliable for bulk rock compositions much richer in MnO. Furthermore, as Mn can occur in several oxidation states in rocks, compositions rich in Mn_2O_3 for example are not suitable for calculations with these models. As with Fe, it is likely that all rocks contain some mixture of MnO and Mn_2O_3, and successful modelling of many rocks may require that small adjustments be made to the bulk rock composition. Such adjustments should be petrographically and geochemically justified, via identification of Mn in phases in which it is likely to be in the Mn^{3+} state (e.g. Mn^{3+} in andalusite, epidote/piedmontite) where possible.

Additionally, MnO is not considered in several key high T phases (e.g. melt, sapphirine, osumilite) nor has the veracity of the Mn-end-member and mixing properties been tested at these conditions. Calculated phase equilibria at higher T conditions could be erroneous, at least until Mn is incorporated in the thermodynamic descriptions of these phases.

Despite the considerable progress in the development of a–x relations for complex multi-component minerals over the last ten years (e.g. White $et\ al.$, 2007; Green $et\ al.$, 2007; Diener $et\ al.$ 2007; Tajčmanová, et al., 2009; Diener & Powell, 2012) there remain considerable chalenges and inconsistencies. As discusssed in White $et\ al.$ (2014) the

persistence of margarite-bearing fields in common metapelite compositions represents one such challenge, and it would appear at this stage that an appraisal of how the Na_2O–CaO–K_2O-bearing phases (mica feldspar and epidote) are interacting in the large systems is required. In addition to uncertainties associated with the a–x relations themselves, there are considerable uncertainties regarding oxidation state of several key elements including Mn. To these may be added many geologically-based sources of uncertainty such as in relation to equilibrium volume, including fractionation of components into porphyroblast cores, composition of co-existing fluids and open system behaviour. Given these caveats interpretations that use the results literally, such as to interpret the degree of overstep of reactions based on intersecting compositional isopleths are unlikely to be defensible. Thus, the a–x relations presented here and phase diagrams produced from their use are better thought of as a thermodynamic framework in which to interpret metamorphic features rather than a literal and absolute solution. However, these limitations should not prevent the quantitative assessment of metamorphic conditions, but rather should prompt an appropriate degree of uncertainty to be attached to such results.

Acknowledgements

References

Ague, J.J., 1991. Evidence for major mass transfer and volume strain during regional metamorphism of pelites *Geology*, **19**, 855–858.

Albee, A.L., 1965. A petrogenetic grid for the Fe-Mg silicates of pelitic schists. *American Journal of Science*, **263**, 512–536.

Álvarez-Valero, A.M., Cesare, B. & Kriegsman, L.M., 2007. Formation of spinel-cordierite-feldspar-glass coronas after garnet in metapelitic xenoliths: reaction modelling and geodynamic implications. *Journal of Metamorphic Geology*, **25**, 305–320.

Atherton, M.P., 1964. The garnet isograd in pelitic rocks and its relationship to metamorphic facies. *American Mineralogist* **49**, 1331–1349.

Atherton, M.P., 1968. The variation in garnet, biotite and chlorite composition in medium grade pelitic rocks from the Dalradian, Scotland, with particular reference to the zonation in garnet. *Contributions to Mineralogy and Petrology*, **18**, 347–371.

Atherton, M.P. & Brotherton, M.S., 1982. Major element composition of the pelites of the Scottish Dalradian. *Geological Journal*, **17**, 185–221.

Bickle, M.J. & Archibald, N.J., 1984. Chloritoid and staurolite stability: implications for metamorphism in the Archaean Yilgarn Block, Western Australia. *Journal of Metamorphic Geology*, **2**, 179–203.

Blümel, P. & Schreyer, W., 1977. Phase relations in pelitic and psammitic Gneisses of the sillimanite–potash feldspar and cordierite–potash feldspar zones of the Moldanubicum of the Lam–Bodenmaiz area, Bavaria. *Journal of Petrology*, **18**, 431–459.

Bosse, V., Ballevre, M. & Vidal, O., 2002. Ductile thrusting recorded by the garnet isograd from bluesschist facies metapelites of the Ile de Groix, Armorican Massif, France. *Journal of Petrology*, **43**, 485–510.

Chinner, G.A., 1960. Pelitic gneisses with varying ferrous/ferric ratios from Glen Clova, Angus, Scotland. *Journal of Petrology*, **1**, 178–217.

20

Chinner, G.A., 1962. Almandine in thermal aureoles. *Journal of Petrology*, **3**, 316–340.

Chinner, G.A., 1967. Chloritoid and isochemical character of Barrows zones. *Journal of Petrology*, **8**, 268–282.

Dachs, E, Geiger, C.A, Benisek, A., & Grodzicki, M., 2014. Thermodynamic mixing properties of almandine-spessartine solid solutions. *Geochimica et Cosmochimca Acta*, **125**, 210–224.

Davidson, L.R. & Matheson, C.I., 1974. Aluminous orthopyroxenes and associated cordierites, garnets and biotites from granulites of the Quairading district, Western Australia. *Neues Jahrbuch für Mineralogie Monatshefte*, 371–398.

Diener, J.F.A., & Powell, R., 2012. Revised activity–composition models for clinopyroxene and amphibole. *Journal of Metamorphic Geology*, **30**, 131–142.

Diener, J.F.A., Powell, R., White, R.W., & Holland, T.J.B., 2007. A new thermodynamic model for clino- and orthoamphiboles in Na_2O-CaO-FeO-MgO-Al_2O_3-SiO_2-H_2O-O. *Journal of Metamorphic Geology* **25**, 631–656.

Droop, G.T.R. & Harte, B., 1995. The effect of Mn on the phase relations of medium-grade pelites: Constraints from natural assemblages on petrogenetic grid topology. *Journal of Petrology*, **36**, 1549–1578.

Droop, G.T.R. & Moazzen, M., 2007. Contact metamorphism and partial melting of Dalradian pelites and semipelites in the southern sector of the Etive aureole. *Scottish Journal of Geology*, **43**, 155–179.

Engel, A.E.G., & Engel, C.G., 1960. Progressive metamorphism and granitization of the Major Paragneiss, northwest Adirondack Mountains, New York. Part II: mineralogy. *Bulletin of the Geological Society of America*, **71**, 1–58.

Feenstra, A., Peters, T., 1996. Experimental determination of activities in $FeTiO_3 - MnTiO_3$ ilmenite solid solution by redox reversals. *Contributions to Mineralogy and Petrology*, **126**, 109–120.

Fletcher, C.J.N. & Greenwood, H.J., 1979. Metamorphism and structure of Penfold Creek area, near Quesnel Lake, British Columbia. *Journal of Petrology*, **20**, 743–794.

Fraser, G., Worley, B. & Sandiford, M., 2000. High-precision geothermobarometry across the High Himalayan metamorphic sequence, Langtang Valley, Nepal. *Journal of Metamorphic Geology*, **18**, 665–681.

Ghent, E.D. & De Vries, C.D.S., 1972. Plagioclase-garnet-epidote equilibria in hornblende-plagioclase bearing rocks from the Esplanade Range, British Columbia. *Canadian Journal of Earth Sciences*, **9**, 618–635.

Green J.C., 1963. High-level metamorphism of pelitic rocks in northern New Hampshire. *American Mineralogist*, **48**, 991–1023.

Greenfield, J.E., 1997. Migmatite formations at Mt Stafford, central Australia. Unpublished PhD thesis, The University of Sydney, Sydney, Australia.

Grew, E.S., 1981. Granulite facies metamorphism at Molodezhneya station, east Antartica. *Journal of Petrology*, **22**, 297–336.

Guidotti, C.V., 1974. Transition from staurolite to sillimanite zone, Rangely Quadrangle, Maine. *Geological Society of America, Bulletin*, **85**, 475–490.

Harris, N.B.W., 1976. The significance of garnet and cordierite from the Sioux Lookout Region of the English River Gneiss Belt, Northern Ontario. *Contributions to Mineralogy and Petrology*, **55**, 91–104.

Harte, B. & Hudson, N.F.C., 1979. Pelite facies series and the temperature and pressures of Dalradian metamorphism in E. Scotland. In: *The Caledonides if the British Isles - Reviewed* (eds, A.L Harris, C.H. Holland & B.E. Leake), pp. 323–337. Geological Society of London, London.

Hauzenberger, C.A., Mogessie, A., Hoinkes, G. Felfernig, A., Bjerg, E.A., Konstadinoff, J., Delpino, S. & Dimieri, L., 2001. Metamorphic evolution of the Sierras de San Luis, Argentina: granulite facies metamorphism related to mafic intrusions. *Mineralogy and Petrology*, **71**, 95–126.

Heald, M.T., 1950. Structure and petrology of the Lovewell Mountain quadrangle, New Hampshire. *Geological Society of America Bulletin*, **61**, 43–89

Herman, L.L., Shcheka, S.A. & Shuldiner, V.I., 1978. Metamorphic complexes of the Ganalsky Range, Kamchatka. *Pacific Geology*, **13**, 49–64.

Hietanen, A., 1956. Kyanite, andalusite and sillimanite in the schist in Boehls Butte Quadrangle, Idaho. *American Mineralogist*, **41**, 1–27.

Hodges, K.V. & Spear, F.S., 1982. Geothermometry, geobarometry and the Al_2SiO_5 triple point at Mt. Moosilauke, New Hampshire. *American Mineralogist*, **84**, 1118–1134.

Holland, T.J.B., & Powell, R., 1996. Thermodynamics of order–disorder in minerals. 1: symmetric formalism applied to minerals of fixed composition.. *American Mineralogist* **81**, 1413–1424.

Holland, T.J.B., & Powell, R., 1996. Thermodynamics of order–disorder in minerals. 2 symmetric formalism applied to solid solutions.. *American Mineralogist* **81**, 1425–1437.

Holland, T.J.B., Baker, J., & Powell, R., 1998. Mixing properties and activity–composition relationships of chlorites in the system MgO–Al_2O_3–SiO_2–H_2O. *European Journal of Mineralogy*, **10**, 395–406.

Holland, T.J.B. & Powell, R., 1998. An internally-consistent thermodynamic dataset for phases of petrological interest. *Journal of Metamorphic Geology* **16**, 309–344.

Holland, T.J.B., & Powell, R., 2003. Activity–composition relations for phases in petrological calculations: an asymmetric multicomponent formulation. *Contributions to Mineralogy and Petrology*, **145**, 492–501.

Holland, T.J.B., & Powell, R., 2011. An improved and extended internally-consistent thermodynamic dataset for phases of petrological interest, involving a new equation of state for solids. *Journal of Metamorphic Geology*, **29**, 333–383.

Hudson, N.F.C., 1985. Conditions of Dalradian metamorphism in the Buchan area, NE Scotland. *Journal of the Geological Society, London*, **142**, 63–76.

Johnson, T., Brown, M., Gibson, R. & Wing, B., 2004. Spinel-cordierite symplectites replacing andalusite: evidence for melt-assisted diapirism in the Bushveld Complex, South Africa. *Journal of Metamorphic Geology*, **22**, 529–545.

Kamineni, D.C., 1975. Chemical mineralogy of some cordierite-bearing rocks near Yellowknife, Northwest Territories, Canada. *Contributions to Mineralogy and Petrology*, **53**, 293–310.

Kawakami, T., Aoya, M., Wallis, S.R., Lee, J., Terara, K., Wang, Y. & Heizler, M., 2007. Contact metamorphism in the Malashan dome, North Himalayan gneiss domes, southern Tibet: an example of shallow extensional tectonics in the Tethys Himalaya. *Journal of Metamorphic Geology*, **25**, 831–853.

Kays, M.A. & Medaris, L.G., 1976. Petrology of Hara Lake para-gneisses, northeastern Saskatchewan, Canada. *Contributions to Mineralogy and Petrology*, **69**, 141–159.

Kunz, B.E., 2011. A mid crustal metamorphic field gradient in Val Strona di Omegna, Ivrea Zone, Italy: constraints from metabasic rocks. Unpublished Diplom thesis, University of Mainz.

Leake, B.E., 1958 Composition of pelites from Connemara, Co. Galway, Ireland. *Geological Magazine*, **95**, 281–296

Likhanov, I.I., Reverdatto, V.V., Sheplev, V.S., Verschinin, A.E. & Kozlov, P.S., 2001. Contact metamorphism of Fe- and Al-rich graphitic metapelites in the Transangarian region of the Yenisei Ridge, eastern Siberia, Russia. *Lithos*, **58**, 55–80.

Lui, S., 2004. Granulite facies metamorphism and partial melting processes in Wuluma Hills, Arunta Inlier, Northern Territory. Unpublished BSc Hons thesis, The University of Sydney, Sydney, Australia.

Mahar, E.M., Baker, J.M., Powell, R. Holland, T.J.B. & Howell, N., 1997. The effect of Mn on mineral stability in metapelites. *Journal of Metamorphic Geology*, **15**, 223–238.

Mather, J.D., 1970. The biotite isograd and the lower greenschist facies in the Dalradian rocks of Scotland. *Journal of Petrology*, **11**, 253–275.

Miyashiro, A., 1953. Calcium-poor garnet in relation to metamorphism. *Geochimica et Cosmochimica Acta*, **4**, 179–208.

Mposkos, E., 1989. High-pressure metamorphism in gneisses and pelitic schists in the East Rhodope Zone (N. Greece). *Mineralogy and Petrology*, **41**, 25–39.

Novak, J.M. & Holdaway, M.J., 1981. Metamorphic petrology, mineral equilibria and polymetamorphism in the Augusta quadrangle, south-central Maine. *American Mineralogist*, **66**, 51–69.

O'Neill, H.St.C., 1998. Partitioning of Fe and Mn between ilmenite and olivine at $1100°$ C: constraints on the thermodynamic mixing properties of $(Fe, Mn)TiO_3$ ilmenite solid solutions. *Contributions to Mineralogy and Petrology*, **133**, 284–296.

O'Neill, H.St.C., Pownceby, M.I., & Wall, V.J., 1989. Activity-composition relations in $FeTiO_3 - MnTiO_3$ ilmenite solid solutions from emf measurements at 1050–1300K. *Contributions to Mineralogy and Petrology*, **103**, 216–222.

Osberg, P.H., 1971. An equilibrium model for Buchan-type metamorphic rocks, south-central Maine. *American Mineralogist* **56**, 570–586.

Otamendi, J.E., Patiño Douce, A.E. & Demichelis, A.H., 1999. Amphibolite to granulite transition in aluminous greywackes from Sierra de Comechingones, Córdoba, Argentina. *Journal of Metamorphic Geology*, **17**, 415–434.

Patiño Douce, A.E. & Beard, J.S., 1995. Dehydration melting of biotite gneiss and quartz amphibolite from 3 to 15 kbar. *Journal of Petrology*, **36**, 707–738.

Patiño Douce, A.E. & Beard, J.S., 1996. Effects of P, $f(O_2)$ and Mg/Fe ratio on dehydration melting of model metagreywackes. *Journal of Petrology*, **37**, 999–1024.

Patiño Douce, A.E., Johnston, A. D. & Rice, J.M., 1993. Octahedral excess mixing properties in biotite: A working model with applications to geobarometry and geothermometry. *American Mineralogist*, **78**, 113–131.

Pattison, D.R.M. & Tinkham, D.K., 2009. Interplay between equilibrium and kinetics in prograde metamorphism of pelites: an example from the Nelson aureole, British Columbia. *Journal of Metamorphic Geology* **27**, 249–279.

Pattison, D.R.M. & Vogl, J.J., 2005. Contrasting sequences of metapelitic mineral-assemblages in the aureole of the tilted Nelson Batholith, British Columbia:

Implications for phase equilibria and pressure determination in andalusite–sillimanite-type settings. *Canadian Mineralogist*, **43**, 51–88.

Phinney, W.C., 1963. Phase equilibria in the metamorphic rocks of St Paul Island and Cape North, Nova Scotia. *Journal of Petrology*, **4**, 90–130.

Pomroy, N.E., 2004. Formation of metatexite and diatexite in upper amphibolite facies felsic gneiss from Southern Cross, Broken Hill. Unpublished BSc Hons thesis, The University of Melbourne, Melbourne, Australia.

Powell, R., & Holland, T.J.B., 1993. On the formulation of simple mixing models for complex phases *American Mineralogist* **78**, 1174–1180.

Powell, R., & Holland, T.J.B., 1999. Relating formulations of the thermodynamics of mineral solid solutions: activity modelling of pyroxenes, amphiboles and micas. *American Mineralogist*, **84**, 1–14.

Powell, R., & Holland, T.J.B., 2008. On thermobarometry. *Journal of Metamorphic Geology* **26**, 155–180.

Powell, R., Holland, T.J.B. & Worley, B., 1998. Calculating phase diagrams involving solid solutions via non-linear equations, with examples using THERMOCALC. *Journal of Metamorphic Geology*, **16**, 577–588.

Powell, R., White, R., Green, E.C.R., Holland, T.J.B., & Diener, J., 2014. On parameterising thermodynamic descriptions of minerals for petrological calculations. *Journal of Metamorphic Geology*, **31**, 245–260.

Powell, R., Woodhead, J., & Hergt, J., 2002. Improving isochron calculations with robust statistics and the bootstrap. *Chemical Geology* **185**, 191–204.

Pownceby, M.I., Wall, V.J., & O'Neill, H.St.C., 1987. Fe-Mn partitioning between garnet and ilmenite: experimental calibration and applications. *Contributions to Mineralogy and Petrology*, **97**, 116–126.

Redler, C., 2011. Granulite facies metamorphism and partial melting processes in the Ivrea zone, Northern Italy. Unpublished PhD thesis, University of Mainz.

26

716 Reinhardt, E.W., 1968. Phase relations in cordierite-bearing gneisses from the Gananoque
717   area, Ontario. *Canadian Journal of Earth Sciences*, **5**, 455–482.

718 Sevigny, J.H., & Ghent, E.D., 1989. Pressure, temperature and fluid composition during
719   amphibolite facies metamorphism of graphitic metapelites, Howard Ridge, British
720   Columbia. *Journal of Metamorphic Geology*, **7**, 497–505.

721 Spear, F.S. & Cheney, J.T., 1989. A petrogenetic grid for pelitic schists in the system
722   SiO_2–Al_2O_3–FeO–MgO–K_2O–H_2O. *Contributions to Mineralogy and Petrology*, **101**,
723   149–164.

724 Smye, A.J., Greenwood, L.V. & Holland, T.J.B., 2010. Garnet-chloritoid-kyanite
725   assemblages: eclogite facies indicators of subduction constraints in orogenic belts.
726   *Journal of Metamorphic geology*, **28**, 753–768.

727 Stewart, F.H., 1942. Chemical data on a silica-poor argillaceous hornfels and its
728   constituent minerals. *Mineralogical Magazine*, **26**, 260–266.

729 Symmes, G.H. & Ferry, J.M., 1992. The effect of whole-rock MnO content on the stbility
730   of garnet in pelitic schists during metamorphism. *Journal of Metamorphic Geology*,
731   **10**, 221–237.

732 Tajčmanová, L., Connolly, J.A.D., & Cesare, B., 2009. A thermodynamic model for
733   titanium and ferric iron solution in biotite. *Journal of Metamorphic Geology*, **27**,
734   153–165.

735 Thompson, A.B., Lyttle, P.T. & Thompson J.B., 1977. Mineral reactions and A-Na-K
736   and A-F-M facies types in Gassets Schist, Vermont. *American Journal of Science*,
737   **277**, 1124–1151.

738 Tiddy, B.J., 2002. Partial melting and leucosome development in the Southern Cross
739   region, Broken Hill, New South Wales. Unpublished BSc Hons thesis, The University
740   of Melbourne, Melbourne, Australia.

741 Tinkham, D.K. & Ghent, E.D., 2005. Estimating P–T conditions of garnet growth with
742   isochemical phase diagram sections and the problem of effective bulk-composition.
743   *Canadian Mineralogist*, **43**, 35–50.

⁷⁴⁴ Tinkham, D.K., Zuluaga, C.A. & Stowell, H.H., 2001. Metapelite phase equilibria
⁷⁴⁵ modeling in MnNCKFMASH: the effect of variable Al_2O_3 and $Mg/(Mg + Fe)$ on
⁷⁴⁶ mineral stability. *Geological Materials Research*, **3**, 1–42.

⁷⁴⁷ Vielzeuf, D. & Montel, J-M., 1997. Partial melting of metagreywackes. 2. Compositions
⁷⁴⁸ of minerals and melts. *Contributions to Mineralogy and Petrology*, **128**, 176–196.

⁷⁴⁹ Vilà, M., Pin, C. Liesa, M. & Enrique, P., 2007. LPHT metamorphism in a late orogenic
⁷⁵⁰ transpressional setting, Albera Massif, NE Iberia: implications for the geodynamic
⁷⁵¹ evolution of the Variscan Pyrenees. *Journal of Metamorphic Geology*, **25**, 321–347.

⁷⁵² Waters, D.J. & Whales, C.J., 1984. Dehydration melting and the granulite transition in
⁷⁵³ metapelites from southern Namaqualand, S. Africa. *Contributions to Mineralogy and*
⁷⁵⁴ *Petrology*, **88**, 269–275.

⁷⁵⁵ Wei C., Clarke, G.L., Tian, W. & Qiu, L., 2007. Transition of metamorphic series from
⁷⁵⁶ the Kyanite to andalusite-types in the Altai orogen, Xinjiang, China: Evidence from
⁷⁵⁷ petrography and calculated KMnFMASH and KFMASH phase relations. *Lithos*, **96**,
⁷⁵⁸ 353–374.

⁷⁵⁹ West, D.P., Yates, M.G., Gerbi, C. & Barnard, N.Q., 2008. Metamorphosed Ordovician
⁷⁶⁰ Fe- and Mn-rich rocks in south-central Maine: From peri-Gondwanan deposition
⁷⁶¹ through Acadian metamorphism. *American Mineralogist*, **93**, 270-282.

⁷⁶² White, R.W., 1997. The Pressure - Temperature evolution of a granulite facies terrane,
⁷⁶³ western Musgrave Block, central Australia. Unpublished PhD thesis, Macquarie
⁷⁶⁴ University, 257pp.

⁷⁶⁵ White, R.W., Powell, R., Holland, T.J.B. & Worley, B.A., 2000. The effect of TiO_2 and
⁷⁶⁶ Fe_2O_3 on metapelitic assemblages at greenschist and amphibolite facies conditions:
⁷⁶⁷ mineral equilibria calculations in the system $K_2O–FeO–MgO–Al_2O_3–SiO_2–H_2O–$
⁷⁶⁸ $TiO_2–Fe_2O_3$. *Journal of Metamorphic Geology*, **18**, 497–511.

⁷⁶⁹ White, R.W., Powell, R. & Clarke, G.L., 2002. The interpretation of reaction textures in
⁷⁷⁰ Fe-rich metapelitic granulites of the Musgrave Block, central Australia: Constraints
⁷⁷¹ from mineral equilibria calculations in the system $K_2O–FeO–MgO–Al_2O_3–SiO_2–$
⁷⁷² $H_2O–TiO_2–Fe_2O_3$. *Journal of Metamorphic Geology* **20**, 41–55.

White, R.W., Powell, R. & Holland T.J.B., 2007. Progress relating to calculation of partial melting equilibria for metapelites. *Journal of Metamorphic Geology*, **25**, 511–527.

White, R.W., Powell, R., Holland, T.J.B., Johnson, T.E. & Green, E.C.R., 2014. New mineral activity–composition relations for thermodynamic calculations in metapelitic systems. *Journal of Metamorphic Geology*, **31**, 261–286.

Williams, M.L., & Grambling, J.A., 1990. Manganese, ferric iron, and the equilibrium between garnet and biotite. *American Mineralogist*, **75**, 886–908.

APPENDIX 1: Interaction energies

Following the adoption of micro-ϕ for the incorporation of the Mn-end-members in the minerals, as discussed in the text, along with the interaction energies from White *et al.* (2014), the interaction energies W_{ij} in matrix form are:

g	py	gr	kho	spss
alm	2.5	5	22.6	2
py		31	5.4	2
gr			-15.3	0
kho				29.4

chl	afchl	ames	daph	ochl1	ochl4	f3clin	mnchl
clin	17	17	20	30	21	2	15
afchl		16	37	20	4	15	32
ames			30	29	13	19	26
daph				18	33	22	10
ochl1					24	28.6	25
ochl4						19	31
f3clin							17

bi	ann	obi	east	tbi	fbi	mn
phl	12	4	10	30	8	9
ann		8	15	32	13.6	6.3
obi			7	24	5.6	8.1
east				40	1	13
tbi					40	30
fbi						11.6

st	fst	mnst	msto	mstt
mst	16	12	2	20
fst		8	18	36
mnst			14	32
msto				30

ctd	fctd	mnctd	ctdo
mctd	4	3	1
fctd		3	5
mnctd			4

cd	fcrd	hcrd	mncrd
crd	8	0	6
fcrd		9	4
hcrd			6

opx	fs	fm	mgts	fopx	mnopx	odi
en	7	4	$13 - 0.15P$	$11 - 0.15P$	5	$32.2 + 0.12P$
fs		4	$13 - 0.15P$	$11.6 - 0.15P$	4.2	$25.54 + 0.084P$
fm			$17 - 0.15P$	$15 - 0.15P$	5.1	$22.54 + 0.084P$
mgts				1	$12 - 0.15P$	$75.4 - 0.94P$
fopx					$10.6 - 0.15P$	$73.4 - 0.94P$
mnopx						$24.54 + 0.084P$

ilm	dilm	hem	geik	pnt
oilm	15.6	26.6	4	2
dilm		11	4	2
hem			36	25
geik				4

APPENDIX 2: Natural assemblage data

A natural assemblage database has been assembled with the focus on mineral assemblages from rocks with a range of MnO content (see Supplementary material). The analyses given in the supplementary material were taken from the following: 1, Grew (1981) — rutile present; 2, Hauzenberger *et al.* (2001); 3, Sevigny & Ghent (1989); 4, Redler (2011); 5, Kunz (2011); 6, Fraser *et al.* (2000); 7, Bickle & Archibald (1984); 8, Bosse et al. (2002); 9, Blümel & Schreyer (1977); 10, Droop & Moazzen (2007); 11, Álvarez-Valero *et al.* (2007) — El Hoyazo locality; 12, Fletcher & Greenwood (1979); 13, Ghent & De Vries (1972); 14, Greenfield (1997); 15, Grew (1981)— rutile absent; 16, Guidotti (1974) — supp. data; 17, Guidotti (1974); 18, Harris (1976); 19, Hodges & Spear (1982); 20, Kamineni (1975); 21, Kawakami *et al.* (2007); 22, Likhanov *et al.* (2001); 23, Lui (2004); 24, Mather (1970); 25, Álvarez-Valero *et al.* (2007) — Mazarrón locality; 26, Mposkos (1989); 27, Novak & Holdaway (1981); 28, Otamendi *et al.* (1999); 29, Pomroy (2004); 30, Pattison & Vogl (2005); 31, Tiddy (2002); 32, Johnson *et al.* (2004); 33, Vilà *et al.* (2007); 34, West *et al.* (2008); 35, Williams & Grambling, (1990); 36, White (1997); 37, Waters & Whales (1984); 38, Stewart (1942); 39, Thompson *et al.* (1977); 40, Atherton (1968); 41, Heald (1940); 42, Green (1963); 43, Leake (1958); 44, Chinner (1960); 45, Miyashiro (1953); 46, Engel & Engel (1960); 47, Phinney (1963); 48, Albee (1965); 49, Hietanen (1956) 50, Chinner (1967); 51, Reinhardt (1968); 52, Davidson & Matheson (1974); 53, Kays & Medaris (1976); 54, Chinner (1962); 55, Herman et al. (1978); 56, Patiño Douce & Beard (1995); 57, Patiño Douce & Beard (1996); 58, Patiño Douce *et al.* (1993); 59, Vielzeuf & Montel (1997).

A proportion of the data involved wet chemical analyses, with analysed FeO and Fe_2O_3. The data for the remainder of the analyses involve all-Fe-as-FeO. Given the large uncertainties in calculated ferrous-ferric that arise from charge balance calculations (e.g. Powell & Holland, 2008), with the added difficulty of the reliability of stoichiometric constraints for hydrous minerals, the approach followed for analyses involving all-Fe-as-FeO is to adopt heuristics for conversion of FeO to Fe_2O_3: as proportions, cd = 0; ctd = 0.02; g = 0.03; opx = 0.05; chl = 0.1; st = 0.1; and bi = 0.15 (see also the Appendix in White *et al.*, 2014). Given that Mg–Mn exchange reactions are used in the data analysis, the precise values used for the conversion are not important, but it is appropriate to have them in what is considered to be a petrologically consistent order. Charge balance is used to

816 recalculate the ilmenite analyses.

817   Processing of the analyses involves mineral calculation in the commonly-used way, on a

818 specified numnber of oxygens, and assuming the full complement of hydroxyls for the

819 hydrous minerals (except for biotite as a consequence of the oxy-substitution used for Ti).

820 The cations are then used to calculate the composition parameters as defined in the

821 Appendix of White *et al.* (2014). The order parameters, Q, for the Fe–Mg order-disorder

822 in the minerals (and the Mg–Al order-disorder in chlorite) are calculated by solving the

823 appropriate internal equilibria in each mineral using the a-x relations given in Appendix 1,

824 and the ΔH of the internal equilibria given in the Appendix of White *et al.* (2014).

APPENDIX 3: Processing the natural assemblage data

The Mg-Mn exchange reactions can be written in a standard form, involving one cation exchange between minerals A and B, with A–B for Mg–Mn meaning

$$\mathrm{Mn, A + Mg, B = Mg, A + Mn, B}$$
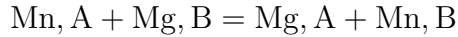
or as an example, g–bi for Mg–Mn meaning that we are considering the equilibrium involving

$$\frac{1}{3}\mathrm{spss, g} + \frac{1}{3}\mathrm{phl, bi} = \frac{1}{3}\mathrm{py, g} + \frac{1}{3}\mathrm{mn, bi}$$
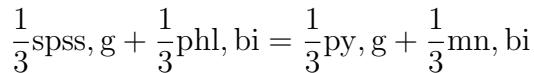
The thermodynamics, in the form $\Delta h = \Delta G^\circ + \mathrm{R}T \ln K$, are evaluated for each such reaction for each appropriate natural assemblage mineral pair. In this, ΔG° is calculated using Holland & Powell (2011), and K is calculated from the compositional and order parameters calculated from the mineral compositions as outlined in Appendix 2. Δh can be thought of as a $\Delta\mathrm{DQF}$ on a one cation exchange basis. Given that the enthalpies of the magnesian end-members are taken to be well-known, Δh relates just to the manganese end-members, e.g. for the above example.

$$\Delta h_{\mathrm{g,bi}} = -\frac{1}{3}\mathrm{DQF}_{\mathrm{spss,g}} + \frac{1}{3}\mathrm{DQF}_{\mathrm{mn,bi}}$$

As noted above, the properties of the pyrophanite and spessartine end-members in the Holland & Powell (2011) dataset are not based on Mahar *et al.* (1997). Therefore, in principle, this means that

$$\Delta h_{\mathrm{g,ilm}} = -\frac{1}{3}\mathrm{DQF}_{\mathrm{spss,g}} + \mathrm{DQF}_{\mathrm{pnt,ilm}} = 0$$

This can be assessed with the database here, and Fig. A3-1a,b shows that this is the case within error (49 data points). In Fig. A3-2, a selection of Δh plots show the nature of the data, the dotted line being the median of the data, the band representing its uncertainty (see below), and the solid line the result of the least squares analysis of all of the data below.

In the following table, n is the number of mineral pairs involved. Δh is the median of the natural assemblage values; $\sigma_{\Delta h}^{\mathrm{distr}}$ is an estimate of the standard deviation on this value using the normalised median absolute deviation, nMAD (e.g. Powell *et al.*, 2002). Medians are used to try and downplay the effect of the scatter and outliers in the data. Treating

$\sigma_{\Delta h}^{\text{distr}}$ now as a Gaussian estimate of standard deviation on the distribution of the data, this divided by the square root of the number of data gives an estimate of the standard deviation on the mean of Δh. This is what would then used to represent the data in the next stage of the data, if the data are homoscedastic, in other words if they are all uncorrelated. But the data are most likely correlated given that they are not individually from separate studies. As a gross approximation to account for this, we use $\sigma_{\Delta h} = 2\sigma_{\Delta h}^{\text{mean}}$, the last column of the following table. That this is appropriate is established *a posteriori* below. the uncertainty bands in Figs A3-1, A3-2 are for $2\sigma_{\Delta h}$

A	B	n	Δh	$\sigma_{\Delta h}^{\text{distr}}$	$2\sigma_{\Delta h}^{\text{mean}}$
g	bi	149	2.623	3.821	0.626
g	chl	22	3.585	6.595	2.812
g	cd	27	4.815	9.239	3.556
g	ctd	25	1.298	4.340	1.736
g	st	47	-0.325	1.661	0.484
g	opx	23	-0.964	4.814	2.008
bi	chl	29	0.490	2.803	1.041
bi	cd	64	-1.639	3.132	0.783
bi	st	43	-1.087	3.308	1.009
bi	opx	52	-6.338	5.661	1.570
chl	cd	8	0.765	1.476	1.044
chl	ctd	13	-5.632	2.628	1.685
chl	st	11	-2.448	1.084	0.654
cd	opx	13	-8.310	4.593	2.548
ctd	st	14	0.180	3.181	1.701

Determining the "best" Δh values from this table is a weighted least squares problem. Assuming that there is no enthalpy modification needed for spessartine, the analysis gives the enthalpy modifications for the individual manganese end-members, on a one cation

basis

	bi	chl	cd	ctd	st	opx
h	-2.63	-2.61	-2.10	0.66	-0.04	3.34

861

862 Multiplied by the number of Mn in the end-member formulae, this gives the DQF of the

863 manganese end-members

	bi	chl	cd	ctd	st	opx
DQF	-7.89	-13.03	-4.21	0.66	-0.17	6.68

864

865 The σ_{fit} of the least squares is 1.24, reflecting that the σ_h used were not inappropriate. The

866 correlation coefficient matrix of the DQF is:

ρ	bi	chl	cd	ctd	st	opx
bi	1	0.429	0.526	0.131	0.337	0.275
chl	0.429	1	0.445	0.267	0.508	0.144
cd	0.526	0.445	1	0.126	0.275	0.232
ctd	0.131	0.267	0.126	1	0.237	0.043
st	0.337	0.508	0.275	0.237	1	0.105
opx	0.275	0.144	0.232	0.043	0.105	1

Casting the least squares result in the original form, we get:

A	B	Δh^{obs}	$2\sigma_{h^{\text{obs}}}$	Δh^{calc}	$2\sigma_{h^{\text{calc}}}$	e	e*
g	bi	2.62	1.25	2.63	1.45	0.01	0.01
g	chl	3.58	5.62	2.61	1.76	−0.98	−0.35
g	cd	4.82	7.11	2.10	2.19	−2.71	−0.76
g	ctd	1.30	3.47	−0.66	3.05	−1.96	−1.13
g	st	−0.32	0.97	0.04	1.24	0.37	0.76
g	opx	−0.96	4.02	−3.34	3.44	−2.38	−1.18
bi	chl	0.49	2.08	−0.02	1.74	−0.51	−0.49
bi	cd	−1.64	1.57	−0.53	1.88	1.11	1.42
bi	st	−1.09	2.02	−2.59	1.56	−1.50	−1.49
bi	opx	−6.34	3.14	−5.97	3.35	0.37	0.23
chl	cd	0.76	2.09	−0.50	2.11	−1.27	−1.21
chl	ctd	−5.63	3.37	−3.27	3.09	2.36	1.40
chl	st	−2.45	1.31	−2.56	1.56	−0.12	−0.18
cd	opx	−8.31	5.10	−5.45	3.63	2.86	1.12
ctd	st	0.18	3.40	0.71	3.01	0.53	0.31

This shows that the fit of the data is good, with $e = \Delta h^{\text{calc}} - \Delta h^{\text{obs}}$ the residuals, and e^*
the residuals normalised to the original specified uncertainties on the data, $\sigma_{h^{\text{obs}}}$.

Figure captions

Fig. 1: Petrogenetic grids in the MnKFMASH system for subsolidus and suprasolidus conditions. The square inset shows the in-excess phases used in the different parts of the diagram. The horizontal ticks on select univariants give the value of m(g) of garnet along the reaction. The set of open triangles at 4.5 kbar indicate the P–T conditions for the AFM compatibility triangles in Fig. 2. The filled triangles at 12 and 6 kbar show the conditions for the MnO–FeO–MgO compatibility triangles in Fig. 3

Fig. 2: Al_2O_3–FeO–MgO (AFM) compatibility triangles for a sequence of temperatures at 4.5 kbar. The MnKFMASH system is reduced to AFM by taking garnet, muscovite, quartz and H_2O to be in excess. The diagrams show the changing divariant to trivariant phase relationships on crossing reactions 3 to 6 (see text for details). The P–T conditions for each compatibility triangle are given on the figure and additionally shown as a series of open triangles in Fig. 1.

Fig. 3: MnO–FeO–MgO compatibility triangles for for conditions either side of reaction 3 at 12 kbar (Fig. 3a, b) and 6 kbar (Fig. 3c, d). The MnKFMASH system is reduced to MnO–FeO–MgO by taking kyanite, muscovite, quartz and H_2O to be in excess and is thus only applicable to aluminous metapelites. The P–T conditions for each compatibility triangle are given on the figure and additionally shown as a series of filled triangles in Fig. 1.

Fig. 4: MnKFMASH pseudosections constructed for three different bulk compositions in terms of the A/AFM and x_{Fe} proportions, which are given on each pseudosection. Each of the pseudosections is calculated for a MnO content of 0.1 mol % and additional garnet-in lines are shown for an MnO content of 0.05 mol % (red dashed line) and for the MnO-free system (solid red line labelled MnO = 0). (a) P–T pseudosection from 0.4 to 12 kbar and 450–950 °C. For the subsolidus calculations, H_2O was taken to be in excess, the H_2O content for the suprasolidus calculations was set such that the assemblage at the solidus was just saturated in H_2O (see Table 1). The bulk rock composition is that from fig. 4 in White *et al.* (2014). (b). P–T pseudosection from 0.4 to 12 kbar and 450–700 °C for a more magnesian composition

than (Fig. 4a) but with the same Al_2O_3 content. (c). P–T pseudosection for a more aluminouse composition but with the same x_{Fe} as Fig. 4b

Fig. 5: MnNCKFMASHTO P–T pseudosection for subsolidus conditions based on the synthetic metapelite composition from fig. 5b in White et al. (2014) but with 0.1 mol% MnO. The garnet-in boundary is shown as a thick red line. Garnet-in boundaries for bulk MnO contents of 0 mol% (thin red line), 0.05 mol % (thin dashed red line) and 0.15 mol % (thin dotted red line) are additionally shown. Several zero mode boundaries are highlighted in colour (see legend for explanation).

Fig. 6: MnNCKFMASHTO P–T pseudosection for subsolidus conditions for a synthetic aluminous metapelite composition. The bulk composition used is that from fig. 7 in White et al. (2014) with 0.1 mol % added. The garnet-in boundary is shown as a thick red line. Garnet-in boundaries for bulk MnO contents of 0 mol% (thin red line), 0.05 mol % (thin dashed red line) and 0.15 mol % (thin dotted red line) are additionally shown. Several zero mode boundaries are highlighted in colour (see legend for explanation).

Fig. 7: MnNCKFMASHTO P–T pseudosection for subsolidus conditions calculated for the average greenschist facies metapelite composition from Ague (1991). The CaO content was reduced slightly to account for the likely presence of apatite in most metapelites. The value for O, representing the Fe_2O_3 component was set at 0.498 mol. %to give a $Fe_2O_3/(FeO + Fe_2O_3)$ value of 0.077. The bulk composition used has 0.284 mol % MnO and garnet is stable throughout much of the diagram. Garnet-in lines are also shown for bulk MnO contents of 0.05 and 0.15 mol %. Several zero mode boundaries are highlighted in colour (see legend for explanation).

Fig. 8: MnNCKFMASHTO P–T pseudosection for subsolidus conditions calculated for the average amphibolite facies metapelite composition from Ague (1991). The value for O, representing the Fe_2O_3 component was set at 0.602 mol. % to give a $Fe_2O_3/(FeO + Fe_2O_3)$ value of 0.081. The bulk composition used has 0.175 mol % MnO and garnet has a smaller stability range than for Fig. 7. Garnet-in lines are also shown for bulk MnO contents of 0.05 and 0.15 mol %. Several zero mode boundaries are highlighted in colour (see legend for explanation).

Fig. 9: MnNCKFMASHTO P–T pseudosection for suprasolidus conditions calculated for the same composition as Fig. 8. The H_2O content was set such that the solidus was just fluid saturated at close to 9 kbar. The garnet-in line for the MnO-free system is also shown as a thin red line labelled MnO $= 0$. Several zero mode boundaries are highlighted in colour (see legend for explanation).

Fig. 10: A T–x_{MnO} (Fig. 10a) and P–x_{MnO} (Fig. 10b) pseudosection based on the greenschist facies metapelite composition presented in Ague (1991). For both diagrams the x axis ranges from MnO $= 0$ mol % at $x = 0$ to MnO $= 0.3$ mol % at $x = 1$ In both diagrams the garnet in line is shown as a thick red line and contours of garnet mode are shown as thin red lines. (a). A T–x_{MnO} pseudosection from 400°C to the wet solidus calculated for a pressure of 6 kbar. (b). A P–x_{MnO} pseudosection for 0.4–10 kbar, calculated for a temperature of 580 °C.

Fig. A3-1 : Plots of Δh versus manganese compositional parameters (m) for garnet–ilmenite pairs. Natural assemblage data, ferric iron not analysed (circles); natural assemblage data, wet chemistry (squares); experimental data, ferric iron not analysed (diamonds). (see text).

Fig. A3-2 : Plots of Δh versus manganese compositional parameters (m). (a–f) select mineral pairs involving garnet with biotite, chloritoid and staurolite. (g–l) select mineral pairs involving biotite with chlorite, cordierite and orthopyroxene. Natural assemblage data, ferric not analysed (circles); natural assemblage data, wet chemistry (squares); experimental data, ferric not analysed (diamonds). (see text).

Table 1: Bulk rock compositions used in the construction of pseudosections

mol. %		H_2O	SiO_2	Al_2O_3	CaO	MgO	FeO	K_2O	Na_2O	TiO_2	MnO	O
Fig. 4a		6.553*	68.691	9.860	—	4.006	7.632	3.157	—	—	0.100	—
Fig. 4b		+	73.509	10.552	—	5.480	6.975	3.378	—	—	0.107	—
Fig. 4c		+	73.509	13.898	—	4.008	5.100	3.378	—	—	0.107	—
Fig. 5		+	73.943	9.442	0.295	3.840	7.522	3.028	0.601	0.658	0.105	0.564
Fig. 6		+	68.477	16.560	0.274	3.556	6.966	2.804	0.557	0.610	0.100	0.098
Fig. 7		+	67.322	12.671	1.558	5.179	7.000	2.929	1.779	0.781	0.284	0.498
Fig. 8		+	64.578	13.651	1.586	5.529	8.025	2.943	2.000	0.907	0.175	0.602
Fig. 9		6.244	60.546	12.799	1.487	5.183	7.524	2.759	1.878	0.850	0.164	0.565
Fig. 10	x=0	+	67.513	12.707	1.563	5.194	7.019	2.938	1.784	0.783	0.000	0.499
Fig. 10	x=1	+	67.311	12.669	1.558	5.178	7.000	2.929	1.779	0.781	0.300	0.497

+, H_2O in excess; *, H_2O taken as in-excess for subsolidus part of diagram

01(mnkfm).pdf

MnKFMASH (+ q ±mu ±ksp ±liq)

P (kbar)

16
15
14
13
12
11
10
9
8
7
6
5
4
3
2
1

m(g) = 0.1
0.2
0.3
0.4
ky ctd
g st chl
0.5
0.6

m(g) = 0.1
st chl
g ky bi
0.2
0.3

and ctd
g st chl
and ctd chl
chl st ctd
g st bi   st chl
g and bi

chl ctd
g and bi
and ctd
g st bi

g sill bi
opx cd liq

chl ctd
g st bi

m(g) = 0.6
g sill chl
cd bi
0.5

m(g) = 0.1

g sill bi
cd liq

0.6
0.5
0.4
0.2
0.3
0.45
X 0.4304
g chl
and cd bi

g mu
and cd bi ksp

g bi liq
opx cd

+mu,
liq

+ mu, H2O

+ksp,
liq

+ksp,
H2O

○ KFMASH
● MnKFMASH
◆ MnKMASH

T (°C)

450   500   550   600   650   700   750   800   850   900   950

(a) 483 ℃ 4.5 kbar ky Al₂O₃ +g +mu +q +H₂O st ctd chl FeO MgO bi

(b) 520 ℃ 4.5 kbar Al₂O₃ +g +mu +q +H₂O st ctd chl FeO MgO bi

(c) 535 ℃ 4.5 kbar Al₂O₃ +g +mu +q +H₂O st chl FeO MgO bi

(d) 570 ℃ 4.5 kbar Al₂O₃ +g +mu +q +H₂O st chl FeO MgO bi

(e) 585 ℃ 4.5 kbar Al₂O₃ +g +mu +q +H₂O cd st chl FeO MgO bi

(f) 589 ℃ 4.5 kbar Al₂O₃ +g +mu +q +H₂O cd st chl FeO MgO bi

(a) MnKFMASH (+ q)

chl

MnO = 0.05
MnO = 0
g chl bi mu H₂O

g bi mu H₂O

g ky ksp liq

g bi mu liq
g bi mu ksp liq
g mu ksp liq

g sill ksp liq

g sill liq

chl bi mu H₂O

g st bi mu H₂O

g sill bi mu H₂O

g sill bi ksp liq

g sill cd ksp liq

g sill cd liq

A/(AFM) = 0.46
XFe = 0.66

g cd ksp liq

g cd bi ksp liq

g sill cd liq

g opx cd ksp liq

and bi mu H₂O

cd bi ksp H₂O

(b) MnKFMASH (+ q + mu +H₂O)

chl

MnO = 0.05
MnO = 0

g chl bi

g bi

chl bi

g st bi

g ky bi

A/(AFM) = 0.46
XFe = 0.56

g sill bi

st bi

sill bi

and bi

and cd bi

cd bi

cd bi ksp (-mu)

(c) MnKFMASH (+ q + mu +H₂O)

A/(AFM) = 0.60
XFe = 0.56

g ctd chl

g st chl

g ky bi

ctd chl

MnO = 0
MnO = 0.05

g st bi

st ctd chl

g st chl bi

g sill st bi

st chl

st bi

g sill bi

and chl

g and bi

g and cd bi

and cd bi

and cd ksp (-mu)

45

05(mnps1).pdf

MnNCKFMASHTO (+mu +q + H2O)

P (kbar)

g chl bi pa ilm hem mt

g chl bi pa ep hem ru

g chl bi pa ep ilm hem

g chl bi pa ilm hem

g bi pa pl ilm hem

g bi pa ilm hem

g bi pa ilm hem mt

g bi pl ilm hem

g chl bi pa ilm mt

g bi pa ilm mt

g bi pl ilm hem mt

g chl bi pa ab ep hem ru

g chl bi pa ep ilm mt

g chl bi ilm mt

g bi ilm mt

g bi pl ilm mt

chl bi ab ep hem ru

chl bi ab ep ilm hem ru

chl bi ab ep ilm mt

g chl bi ab ep ilm mt

g chl bi ep ilm mt

g chl bi ma ilm mt

g st bi ilm mt

g st bi pl ilm mt

g st bi ma ilm mt

g st bi ma pl ilm mt

g sill bi pl ilm mt

MnO=0

MnO=0.05

MnO=0.15

chl bi ab ep ilm mt ru

chl bi ab ep ilm mt

chl bi pl ep ilm mt

g chl bi ma pl ilm mt

g chl bi pl ilm mt

g sill st bi pl ilm mt

sill bi pl ilm mt

chl bi pl ep ilm mt

g st chl bi pl ilm mt

g and bi pl ilm mt

chl bi pl ilm mt

and bi pl ilm mt

and bi ksp pl ilm mt (-mu)

cd and bi ksp pl ilm mt (-mu)

chl bi pl ilm mt

and chl bi pl ilm mt

cd bi ksp pl ilm mt (-mu)

T (°C)

450   500   550   600   650   700

1) g chl bi pa ab ep ru
2) g chl bi ab ep ru
3) g chl bi pa ab ep hem ru
4) g chl bi pa ep ilm hem ru
5) chl bi pa ep ilm hem ru

6) chl bi pa ep ilm hem
7) chl bi pa ab ep ilm hem
8) chl bi ab ep ilm hem
9) chl bi pa ep ilm hem mt

10) chl bi pa ep ilm mt
11) chl bi ab ep ilm hem mt ru
12) chl bi ab ep mt ru
13) g chl bi pl ep ilm mt

14) g st chl bi ma pl ilm mt
15) st bi pl ilm mt
16) g and chl bi pl ilm mt
17) chl bi pl ab ep ilm mt

zero-mode boundaries   garnet   aluminosilicate   chlorite   staurolite

paragonite   margarite   plagioclase   albite   epidote   all others

46

MnNCKFMASHTO (+mu +q + H2O)

P (kbar) vs T (℃)

chl ctd pa ep ru

chl ctd ep ru

g chl ctd ep ru

MnO=0

g st chl ctd ru

g st ru

g ky bi ru

g ky st bi ru

1) g chl ctd ma ep ru

chl ctd ma ep ru

g chl ctd ma ru

g st chl ru

g st bi ru

chl ctd ma ru

MnO=0.15

g st chl ma ru

g st chl ilm ru

5

g st chl ma ilm ru

g st chl ilm

g st bi pl ru

g st bi pl ilm ru

g st bi ilm ru

4

g st bi ilm

g st chl ma ilm

MnO=0.05

g st bi ma ilm

g st bi pl ilm

st chl ctd ma ru

g st chl bi ma ilm

g st chl ma ilm

g st bi ma pl ilm

g sill st bi pl ilm

st chl ma ru

st bi pl ilm

st chl ma ilm ru

st bi ma pl ilm

g sill bi pl ilm

st chl ma ilm

st chl bi ma ilm

11

sill bi pl ilm

and st bi pl ilm

and chl ctd ma ru

6

8

st chl bi ma pl ilm

g and st bi pl ilm

g and bi pl ilm

12

and bi pl ilm

and bi pl ksp ilm (-mu)

and chl ma ru

9

and chl ma ilm

and chl ma pl ilm

and cd bi pl ksp ilm (-mu)

10

and st chl bi pl ilm

and cd pl ksp ilm (-mu)

1) g chl ctd ma ep ru
2) g ky st ru
3) g ky ru
4) g st chl bi ilm
5) gst chl bi ilm ru

6) and st chl ma ru
7) and chl ma ilm ru
8) and st chl ma ilm
9) and chl ma pl ilm
10) and chl pl ilm

11) st chl bi ma pl ilm
12) g and chl bi pl ilm
zero-mode boundaries

— staurolite
— chlorite
— biotite
— garnet
— aluminosilicate

— margarite
— plagioclase
— albite
— paragonite
— chloritoid

— epidote
— all others

47

Figure 6:

MnNCKFMASHTO (+mu +q + H2O)

P (kbar)

T (°C)

MnO=0.05
MnO=0.15

g chl bi pa ep hem ru

g bi pa ep hem ru

g bi pa pl hem ru

1
g chl bi pa ep sph ru
g chl bi pa ab ep sph
g chl bi pa ep ru
g chl bi pa ep ilm ru

g chl bi pa ep ilm hem ru

6
7
g bi pl hem ru
g bi pl ilm hem ru

g chl pa ab ep sph
2
g chl bi pa ab ep sph ru
g chl bi pa ab ep ru

g bi pa ep ilm ru
g bi pl ep ilm ru
g bi pa pl ilm ru
g bi pl ilm ru

3
g chl bi pa ab ep ru
g chl bi pa ab ep ilm ru

g bi pa ep ilm
g bi pa pl ep ilm
g bi pa pl ilm
8
g ky st bi pl ilm
g ky bi pl ilm

4
g chl bi ab ep sph ilm
5
g chl bi ab ep ru
g chl bi ab ep ru

g chl bi pa ep ilm
g bi pa ma pl ilm
g st bi pl ilm

14
13
11
9
g bi pa ma pl ilm mt
g st bi pa ma pl ilm mt

g chl bi ab ep ilm ru
15
g chl bi pl ep ilm
12
g chl bi pl ep ilm mt
10
g st bi pl ilm mt

g sill bi pl ilm

g chl bi pl ilm mt
g st chl bi pl ilm mt
g sill st bi pl ilm mt
g sill bi pl ilm mt

g chl bi pl ab ep ilm
g chl bi pl ep ilm

16
17
18
g chl bi pl ilm

g and bi pl ilm mt

g and bi pl ksp ilm
g and bi pl ksp ilm (-mu)

chl bi pl ab ilm
g and bi pl ilm

and cd bi pl ksp ilm (-mu)

chl bi pl ab ilm mt
g chl bi pl ab ilm mt
and cd bi pl ksp ilm (-mu)

g and cd bi pl ilm
and cd bi pl ilm

1) g chl bi pa ep sph
2) g chl pa ab ep sph ru
3) g chl ab ep sph ru
4) g chl ab ep sph
5) g chl bi ab ep sph

6) g bi pa hem ru
7) g bi pa pl ep ilm hem ru
8) g bi pl ilm
9) g st bi pa ma pl ilm mt
10) g st bi ma pl ilm mt

11) g chl bi pa ma pl ilm mt
12) g chl bi ma pl ilm mt
13) g chl bi pa pl ep ilm
14) g chl bi pa ab ep ilm
15) g chl bi ab ep ilm

16) g chl bi pl ab ep ilm ru
17) g chl bi pl ab ep ru
18) g chl bi pl ab ilm

zero-mode boundaries ── garnet ── aluminosilicate ── chlorite ── staurolite

─── paragonite ─── margarite ─── plagioclase ─── albite ── epidote ── all others

MnNCKFMASHTO (+mu +q + H2O)

1) g chl bi pa ep sph
2) g chl bi pa ab ep sph
3) g chl pa ab ep sph
4) chl ab ep sph ru
5) chl bi ab ep sph ru

6) g chl bi pa ep hem ru
7) g bi pa ep hem ru
8) g bi pa ep ilm hem ru
9) g chl bi pa pl ab ep ilm
10) g chl bi pl ab ep ilm

11) g chl bi pl ep ilm mt
12) g chl bi pa pl ep ilm
13) g chl bi pa ma ep ilm
14) g bi pa ma ep ilm mt
15) g bi pa ma pl ep ilm mt

16) g st chl bi pa pl ilm mt
17) chl bi pl ab ep ilm ru
18) chl bi pl ab ep ilm
19) chl bi pl ep ilm mt
20) and cd bi pl ilm mt

zero-mode boundaries ——— garnet ——— aluminosilicate ——— chlorite ——— staurolite ——— biotite

——— paragonite ——— margarite ——— plagioclase ——— albite ——— epidote ——— all others

49

MnNCKFMASHTO

P (kbar)

T (°C)

1 2 3

g ky bi mu
pl ilm ru q

g ky bi mu
pl ilm ru q liq

g ky bi ksp
pl ilm ru q liq

g ky ksp pl ilm ru q liq

g ky bi mu ksp pl ilm q liq

g ky bi ksp pl ilm q liq

g ky bi mu
pl ilm q

g ky bi mu
pl ilm q liq

g ky st
bi mu pl
ilm q

7

g sill ksp pl ilm q liq

MnO=0

g ky bi mu ksp pl ilm q liq

g sill bi ksp pl ilm q liq

4

5

6

g sill bi mu
pl ilm q liq

g sill bi mu ksp pl ilm q liq

g sill bi mu
pl ilm q H$_2$O

g sill bi mu
pl ilm q liq

g sill cd bi ksp pl ilm q liq

g sill cd ksp pl ilm q liq

9 10

sill bi mu
pl ilm
q H$_2$O

sill bi
ksp pl
ilm q liq

g sill bi pl
ilm q liq

g sill bi
ksp pl ilm mt q liq

g cd ksp pl ilm q liq

8

g cd sp pl
ilm q liq

g cd ksp pl
ilm mt q liq

g cd ksp pl
ilm mt liq

11

18

g sill cd bi ksp pl ilm mt q liq

g cd bi ksp
pl ilm mt q liq

12

19

sill cd bi ksp
pl ilm mt q liq

g opx cd bi ksp
pl ilm mt q liq

g opx cd sp ksp
pl ilm mt liq

g opx
cd sp pl
ilm mt liq

20

cd bi ksp pl ilm mt q liq H$_2$O

cd bi ksp
pl ilm mt q liq

opx cd
bi ksp pl ilm
mt q liq

g opx
cd bi ksp
pl ilm mt liq

g opx cd
ksp pl
ilm mt liq

opx cd ksp pl
ilm mt liq

g opx cd
pl ilm
mt liq

13

cd bi ksp
pl ilm mt q H$_2$O

opx cd bi ksp
pl ilm mt liq

opx cd pl
ilm mt liq

16 15

14

17

opx cd ksp pl ilm mt liq H$_2$O

opx cd pl ilm mt liq H$_2$O

1) g bi mu pl ilm ru q
2) g bi mu pl ilm ru q liq
3) g ky bi mu ksp pl ilm ru q liq
4) g st bi mu pl ilm q
5) g st bi mu pl ilm q H$_2$O

6) g ky st bi mu pl ilm q H$_2$O
7) g ky bi mu pl ilm q H$_2$O
8) g cd ksp pl ilm liq
9) g sill cd ksp pl ilm liq
10) g sill cd sp ksp pl ilm liq

11) g cd sp ksp pl ilm mt liq
12) g cd sp pl ilm mt liq
13) opx cd sp pl ilm mt liq
14) opx cd bi pl ilm mt liq
15) opx cd bi ksp pl ilm mt liq H$_2$O

16) cd bi ksp pl ilm mt liq
17) opx cd bi ksp pl ilm mt q H$_2$O
18) sill bi pl ilm q liq
19) sill cd bi ksp pl ilm q liq
20) sill cd bi ksp pl ilm q H$_2$O

zero-mode boundaries —— garnet —— orthopyroxene —— aluminosilicate ‒‒ cordierite —— spinel —— staurolite
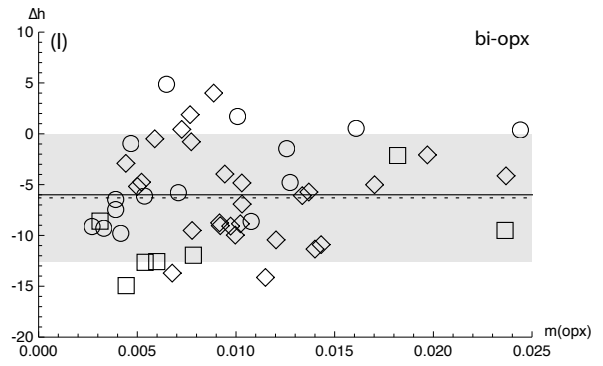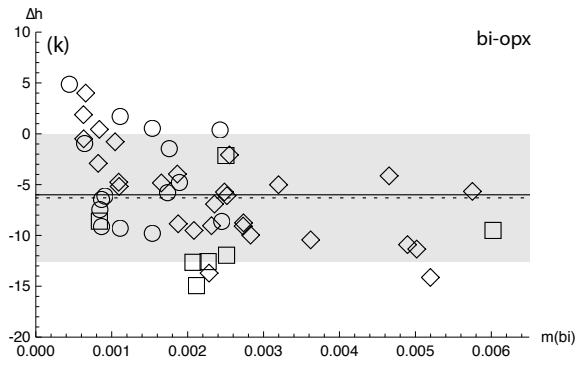‒‒ biotite ‒‒ quartz —— all others

(a)

MnNCKFMASHTO (+mu +q + H2O)

700

650

600

550

500

450

400

T (°C)

sill bi pl ilm

% g   0.4   0.6   0.8   1.0   1.5   2.0

sill bi pl ilm mt

g sill bi pl ilm

2.5

sill st bi pl ilm mt

g sill bi pl ilm mt

0.4   1.0   1.5   2.0   2.5

st bi pl ilm mt

g st bi pl ilm

g st bi pl ilm mt

st bi ma pl ilm mt

3.0

g st bi pa ma pl ilm mt

bi pa ma pl ilm mt

g bi pa ma pl ilm mt

chl bi pa ma pl ilm mt

g chl bi pa ma pl ilm mt

chl bi ma pl ilm mt

g chl bi ma pl ilm mt

2.5

g chl bi pl ep ilm mt

chl bi pl ep ilm

g chl bi pl ep ilm

1.5

chl bi ab ep ilm

g chl bi ab ep ilm

chl bi ab ep ilm ru

g chl bi ab ep ilm ru

chl bi ab ep ru

g chl bi ab ep ru

0.4   0.6   0.8   1.0

chl bi ab ep sph ru

g chl bi ab ep sph ru

chl bi ab ep sph

g chl bi ab ep sph

chl ab ep sph

g chl ab ep sph

XMnO 0   0.1   0.2   0.3   0.4   0.5   0.6   0.7   0.8   0.9   1
MnO 0   0.03   0.06   0.09   0.12   0.15   0.18   0.21   0.24   0.27   0.3
mol%

(b)

MnNCKFMASHTO (+mu +q + H2O)

10

9

8

7

6

5

4

3

2

1

P (kbar)

g bi pa ep ilm ru

g bi pa ep ilm

5.0

g bi pa ma ep ilm mt

g bi pa ma pl ep ilm

g bi pa pl ep ilm

bi pa ma pl ilm mt

g bi pa ma pl ep ilm mt

4.0

g bi pa ma pl ilm mt

0.4   0.6   0.8   1.0   1.5   2.0   2.5   3.0

g st bi pa ma pl ilm mt

st bi ma pl ilm mt

g st bi ma pl ilm mt

st bi pl ilm mt

g st bi pl ilm mt

sill st bi pl ilm mt

g sill st bi pl ilm mt

sill bi pl ilm mt

g sill bi pl ilm mt

and bi pl ilm mt

g and bi pl ilm mt

1.0

and bi pl ilm

0.8

g and bi pl ilm

0.6

0.4

and bi ksp pl ilm (-mu)

and cd bi ksp pl ilm (-mu)

cd bi ksp pl ilm (-mu)

XMnO 0   0.1   0.2   0.3   0.4   0.5   0.6   0.7   0.8   0.9   1
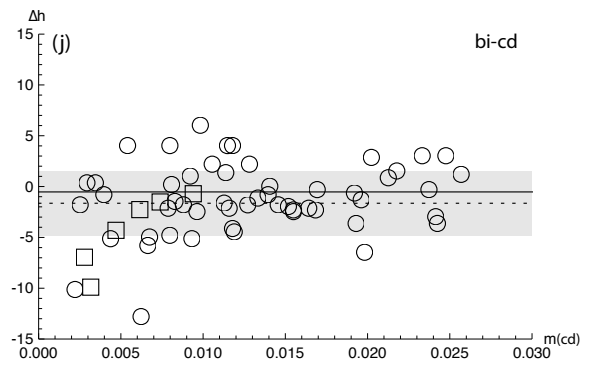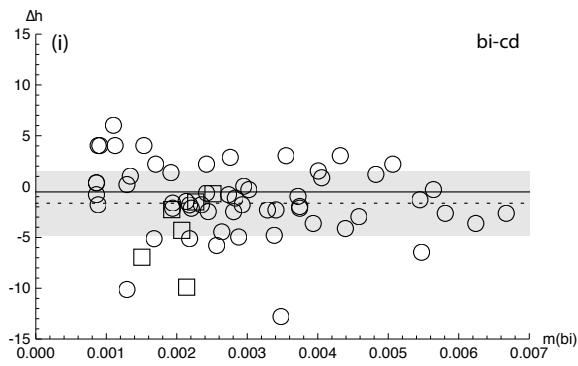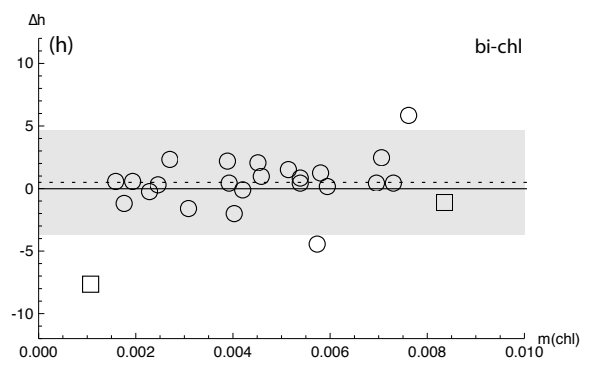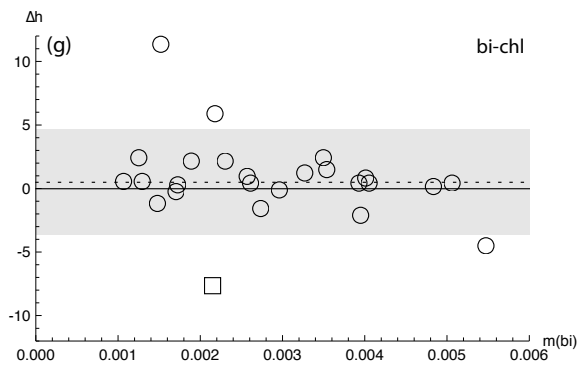MnO 0   0.03   0.06   0.09   0.12   0.15   0.18   0.21   0.24   0.27   0.3
mol%

White et al fig. 3-1

White et al fig. 3-2

White et al fig. 3-2 - cont.